Pore-Scale Modeling of Fluid Transport in Disordered Fibrous Materials

Karsten E. Thompson
Gordon A. and Mary Cain Dept. of Chemical Engineering, Louisiana State University, Baton Rouge, LA 70803

The modeling of fluid transport in fibrous materials is important for many applications. Most models operate at the continuum level, which requires an a priori knowledge of spatially averaged transport parameters. Alternatively, highly detailed models, in which the momentum equations are solved directly, require major simplifying assumptions. Thus, it is desirable to use intermediate-level techniques that model transport using first principles, but that are appropriate for real engineering processes. In this work, pore-scale network modeling is adapted for fibrous materials and tested for a large range of fibrous structures and solid volume fractions. A novel technique is used to generate prototype network structures from Voronoi diagrams. The Voronoi networks are coupled with two different multiphase flow algorithms, enabling the modeling of various displacement processes relevant to engineering. Permeability predictions agree well with known values. Effects of dynamics, wettability, and material structure on displacement were studied. This modeling technique not only allows for better quantification of how microscale properties affect macroscopic transport, but helps reduce the number of experiments required to predict continuum transport parameters for various materials and processes.

Introduction

Natural and manufactured fibrous materials are found in many processes of interest to chemical engineers, including the synthesis of composite materials, filtration, pulp and paper processing, biological transport phenomena, and the design and manufacture of adsorbent materials. Fluid transport is usually modeled using a continuum approach because of the length scales involved and the complexity of real pore structures. Continuum methods are very effective if appropriate averaged parameters are known or can be easily predicted. Oftentimes, however, these parameters can be found only through experiment, most notably in cases where the macroscopic parameters of interest depend strongly on pore-scale behavior. This limitation is important because it can prevent factors such as pore structure, wettability variations, or interface behavior from being explicitly incorporated into a model. A second concern in continuum modeling is the proper choice of scales. Averaged parameters contain implicitly assumed length scales, and a model must operate over similar scales. If the length scale for transport is too small, an averaged parameter is not meaningful. While this problem is rarely apparent for parameters such as porosity or flux, dispersion can exhibit so-called anomalous behavior that makes the determination of characteristic lengths (for dispersion coefficients) difficult. At the other extreme, if the length scale in a model is large compared to the scale over which a parameter varies, then upscaling is required. This problem is common in numerical modeling, where the discretization scale (such as the size of a finite element) is large relative to the scale for permeability variations.

The purpose of pore-scale modeling is to provide a link between microscopic properties of a porous medium and transport behavior at a larger scale. Pore-scale models are an important complement to continuum modeling because they can be used to predict continuum parameters (if they are quantitative), and they provide a means for studying the scaling issues just mentioned. In an ideal modeling scenario, flow

would be modeled at the pore scale using first principles, and the results would be used to generate averaged parameters for use at the continuum level. While this multiscale approach will probably become common in the future, a number of issues must be addressed before it becomes practical. One issue is the ability to consistently generate quantitative transport parameters using only basic morphologic information. This predictive capability has been demonstrated for specific media such as sphere packs (Bryant and Blunt, 1992; Bryant et al., 1993a; Thompson and Fogler, 1997), and certain consolidated rocks (Bryant et al., 1993b; Bakke and Oren, 1997), but not for arbitrary types of media. A second issue is upscaling from the pore to the continuum level. The mathematical and numerical problems are quite challenging because of scaling, computational requirements, history dependence, and so on.

In this article, we apply network modeling to the problem of flow in disordered fibrous materials. A number of advantages are realized by the network approach. First, the resolution allows one to explicitly account for detailed pore structure. Second, methods for the dynamic modeling of multiphase flow are quite well developed. Third, the efficiency of network modeling allows one to operate in reasonably large domains while at the same time including nearly arbitrary types of heterogeneity and disorder.

Background

In general, pore-scale modeling is limited by two major factors. First, the detailed pore structure of real materials is rarely known (aside from what can be described in a statistical sense). Exceptions are cases where microtomography or microscopy has been applied to a small representative volume (Spanne et al., 1994; Coles et al., 1998). Second, even if the detailed pore structure is known, obtaining general solutions to the equations of motion in these complex pore geometries is difficult. Hence, methods for pore-scale modeling employ significant approximation in describing structure and/or fluid mechanics. Of course, the choice of where and how to make simplifications in a model affects what type of information one can expect to gain from it.

Detailed modeling flow in fibrous materials

One of the simplest structures used to represent fibrous materials is a bank of parallel cylinders. This geometry is of interest in composite materials processing for applications in which fluid is injected into preforms that have arrays of parallel fibers (Bafna and Baird, 1992). Sangani and Acrivos (1982) obtained a numerical solution for transverse flow in periodic arrays, as well as analytic expressions for the high and low solid-volume-fraction (SVF) limits. Larson and Higdon (1987) studied Stokes flow in periodic arrays near a plane-porous boundary. Their solution method employed periodicity in the lattice structure, but captured nonperiodic flow behavior in the direction normal to the boundary, thus allowing effects of the plane-porous boundary to propagate into the medium.

Solving the flow in disordered parallel cylinders is more difficult. Sangani and Yao (1988) solved the equations for the stream function and vorticity using the periodic singular solution to the Laplace equation. At the time, computational limitations restricted their solutions to between 9 and 16 cylinders, depending on the porosity. Later, Sangani and Mo (1994) used a multipole approach with lubrication terms to account for forces in narrow gaps between particles. Using this more efficient technique, nondimensional drags were computed for various configurations having up to 64 random cylinders. Koch and Ladd (1997) used the lattice Boltzmann method to examine finite-Reynolds-number flow through random arrays of up to 128 cylinders, showing important transient effects and orientation effects when inertial terms were present. Verberg and Ladd (1999) used a time-independent lattice-Boltzmann method to model low-Reynolds-number flow in arrays of up to 790 cylinders. Liu and Thompson (2002) used domain decomposition to model Stokes flow through highly disordered lattices having arbitrary size distribution and porosity. They show results with up to 1,000 parallel cylinders.

In three dimensions, rigorous solutions for flow at the microscale become much more difficult. Higdon and Ford (1996) modeled three-dimensional Stokes flow in three different periodic fiber lattices using a spectral boundary element method. They report dimensionless permeabilities over the entire range of viable SVF. Although their fiber structures are idealized, the results provide valuable insight into permeability vs. porosity behavior and a good base line for other models since their results are essentially exact. Clague and Phillips (1997) determined the permeability of three-dimensional arrays of dilute nonoverlapping fibers. A numerical technique was used in which each fiber was represented as a line distribution of point forces, and the no-slip condition was enforced in integral form. Although they report results mainly for dilute volume fractions, they note that the method can be used for more concentrated suspensions with the addition of quadropole terms and by using additional point singularities on the particle surfaces, as described by Dabros (1985).

Network models

The main disadvantage of methods for the direct solution of the momentum equation in a porous media, is the intensive computational requirement, which imposes limits on size, structure, and/or porosity. Additionally, most methods are restricted to a single-phase flow, with multiphase lattice-Boltzmann methods being one exception (for example, Gunstensen and Rothman, 1993; Martys and Chen, 1996). Network models are therefore an important alternative because they can be used with large, heterogeneous materials at the expense of a simplified view of the fluid dynamics.

Although modern network models are being used with very complex pore structures (Bakke and Oren, 1997; Liang et al., 2000), the pore space must ultimately be discretized into an interconnected set of pores and pore throats. By assigning hydraulic conductivities to pore throats, the flow problem can then be cast as a pipe network (or resistor network) problem. In short, a mass conservation equation is written for each pore in the network, which produces a set of linear equations that can be solved for individual pore pressures. Clearly, this approach requires nontrivial assumptions to be made. For example, in many porous media the distinction between pores

and pore throats is ambiguous. Similarly, the simple relationship between discrete nodal pressures and flow is a simplification of the true dynamics.

Experience has shown that the advantages of network modeling far outweigh these limitations in many cases. Detailed multiphase algorithms are routinely run on networks of hundreds or thousands of pores. Single-phase flow and solute transport problems can be modeled efficiently using networks of tens of thousands of pores. Network modeling of flow in a porous media is attributed to Fatt (1956). His work has been built upon in evolutionary steps, including the use of random networks (Jerauld et al., 1984; Blunt and King, 1991), the incorporation of detailed fluid mechanics (Koplik, 1982; Goode and Ramakrishnan, 1993), dynamic modeling of multiphase flow (Koplik and Lasseter, 1985; Lenormand et al., 1988; Mogensen and Stenby, 1998), and the development of improved tools for generating realistic networks (Bakke and Oren, 1997; Liang et al., 2000). Network models have facilitated investigations of complex phenomena such as blob mobilization (Dias and Payatakes, 1986), reactive flows (Hoefner and Fogler, 1988; Fredd and Fogler, 1998), flow maldistribution (Thompson and Fogler, 1997), non-Darcy flow (Thauvin and Mohanty, 1998), and interfacial mass transfer (Dillard and Blunt, 2000).

The most important trend during the past ten years has been an increased emphasis on quantitative and predictive modeling. Developments in this area have become possible due, in large part, to new methods for capturing realistic pore morphology in network structures and improved flow algorithms. One of the most important developments was made by Bryant et al. (1993b), who used the term "physically representative network model" to describe a network that retains the dimensionality, structure, and spatial correlation of a real material (a three-dimensional sphere packing in their work). Since then, a number of other models have followed in which the network structure is derived directly from a well-characterized material (real or computer generated), rather than derived from statistics (Bakke and Oren, 1997; Thompson and Fogler, 1997; Fredd and Fogler, 1998; Liang et al., 2000; Hilpert and Miller, 2001). The implications of using a physically representative network model (or variant on this theme) are important. The true three-dimensional pore structure and spatial correlation are implicitly captured in the network, leaving no room to incorporate scaling or adjustable parameters. Bryant et al. (1993a) demonstrated that spatial correlation affects macroscopic transport and, more importantly, that the observed effects could not be reproduced with an equivalent statistically generated model. Fredd and Fogler (1998) used both traditional and physically representative network models to simulate porous media dissolution. While qualitative differences related to the Damkohler number were predicted with a traditional (two-dimensional) model, a physically representative model was required to reproduce experimentally observed effects that were specific to the fluid type used for dissolution.

Generation of network structures

Networks used in network modeling are typically obtained from one of three different ways. Most commonly, interconnected lattices are transformed into flow networks by selecting bond and node sizes from a specified size distribution. These networks are easy to generate and can reproduce certain properties of real materials in a statistical sense (Lowry and Miller, 1995). A second approach is to use a simulated porous medium to construct the network. The advantage is that a simulated medium more readily captures important structural attributes and spatial correlation than a mathematical distribution. This approach also eliminates the use of scaling parameters if the true dimensionality of the model is transferred to the network. For granular media, the most common starting points are computer-generated sphere packings. For consolidated materials, techniques have been developed to simulate the relevant diagenetic steps (Bryant et al., 1993b; Bakke and Oren, 1997; Liang et al., 2000). The third approach is the construction of the network from direct analysis of a real material. Examples include SEM analysis of thin sections (Koplik et al., 1984; Ghassemzadeh et al., 2001), or microtomography, which is a rapidly growing field (Martys, 1996; Coles, 1998). Bryant et al. (1993b) used somewhat of a hybrid of the second and third approaches: Data from the Finney packing (Finney, 1970) were used to model the medium, but the network was generated using a Delaunay tessellation, and computer-simulated compaction and grain growth were employed to mimic consolidation of the medium.

Clearly, the more direct a mapping can be of a real material, the better. However, because of the experimentally intensive procedures required to obtain real mappings, computer simulation methods that attempt to reproduce real pore structure are good compromises.

Network models of fibrous materials

Network modeling has been applied mainly to granular materials or nongranular consolidated rocks in the fields of petroleum engineering and groundwater hydrology. These materials have significantly different structures than fibrous materials. Specifically, solid volume fractions in granular and consolidated media are usually between 0.6 and 0.85. In these structures, it can be argued that the pore and pore-throat idealization is reasonably good. In contrast, fibrous materials are composed of high-aspect-ratio particles, anisotropy is common, and measured SVF spans nearly three orders of magnitude (Jackson and James, 1986).

For these reasons, network modeling has not been used to model fluid flow in fibrous materials until the last few years. Ghassemzadeh et al. (2001) used a network model to study the forced imbibition of a coating fluid into paper. The detailed pore structure of the paper of interest was obtained by SEM imaging, and then mapped onto a flow network. The forced imbibition process was modeled using a dynamic algorithm, with boundary conditions obtained from a macroscopic model of the external flow.

This article describes a more general framework for modeling flow in various types of fibrous materials using a network approach. A method for creating computer-simulated prototype materials is presented in which the pore structure and larger-scale structure can easily be controlled. The transport model is not specific to this prototype model, so it can be integrated with networks from either simulated or real materials. The importance of this approach is that it allows one to

quantify how fluid transport is affected by pore structure, spatial correlation, wettability, solid volume fraction, fluid properties, and flow rate.

Prototype Model of Fibrous Materials

A number of methods have been suggested for the mathematical construction of model fibrous materials (for example, Ethier, 1991; Schweers and Loffler, 1994; Higdon and Ford, 1996; Qi and Uesaka, 1996; Qi, 1997; Clague and Phillips, 1997; Termonia, 1998; Li and Park, 1999). These techniques predominantly characterize the material by a description of the fiber locations and orientations, which presents a significant hurdle for network modeling because the void space must still be mapped onto a discretized, interconnected network. The equivalent problem for sphere packings is handled using a Delaunay tessellation, but no analog for fibrous materials has been suggested. Options such as medial-axis analysis (for example, Lindquist et al., 1996) would be viable in theory. However, the computational requirements of this approach would offset the gains in simplicity and efficiency that one achieves using a computer-generated material in the first place.

These issues were considered when developing a prototype model of fibrous materials. Specifically, the method should allow for efficient generation of various material structures, and lend itself easily to forming the discretized, interconnected framework required in network modeling. The prototype model used here is based on a three-dimensional Voronoi diagram, where the edges of the Voronoi polyhedrons are viewed as fiber segments. The model is not intended to represent any one real fiber. Rather, it has certain characteristics important to fibrous materials: long, slender particles and arbitrarily high SVFs. Furthermore, because a Voronoi diagram is used as the base structure, the pore interconnectivity is defined naturally and uniquely (once fiber diameter is specified), thus requiring few additional transformations prior to flow modeling. This approach is valuable because morphologic properties can be quickly and easily varied to assess their impact on fluid transport.

Voronoi diagrams

A Voronoi diagram is constructed around a set of base points that are random or disordered for most applications. Voronoi diagrams have been used for applications such as modeling foams (Shulmeister et al., 1998), quantifying transport in heterogeneous materials (Jerauld et al., 1984; Sahimi and Tsotsis, 1997), and studying multiphase flow in a porous media (Blunt and King, 1991). In three dimensions, it is a set of space-filling, nonoverlapping polyhedrons; each polyhedron surrounds a base point, and all the space within a given polyhedron is closer to its associated base point than any other. The polyhedrons share planar faces with neighboring polyhedrons. Figure 1a shows a small domain containing randomly placed base points. Figure 1b shows the three-dimensional, periodic Voronoi diagram built around these base points.

To form the prototype fiber network, the edges of the polyhedrons (that is, the black bonds in Figure 1b) are viewed as short fiber segments, to which are assigned finite radii. The cagelike polyhedrons are pores in the network, while the shared faces of neighboring polyhedrons (which are constrictions that lead from one pore to another) are viewed as the pore throats. The radii assigned to the fiber segments dictate the SVF (ϕ) of the porous material; as these radii increase, the SVF increases. At the same time, smaller pore throats are closed off, causing the average coordination number to decrease. The fiber volume fraction can be varied from zero to some upper limit at which no percolation pathway exists in the network. Networks having SVF = 0 can be used for

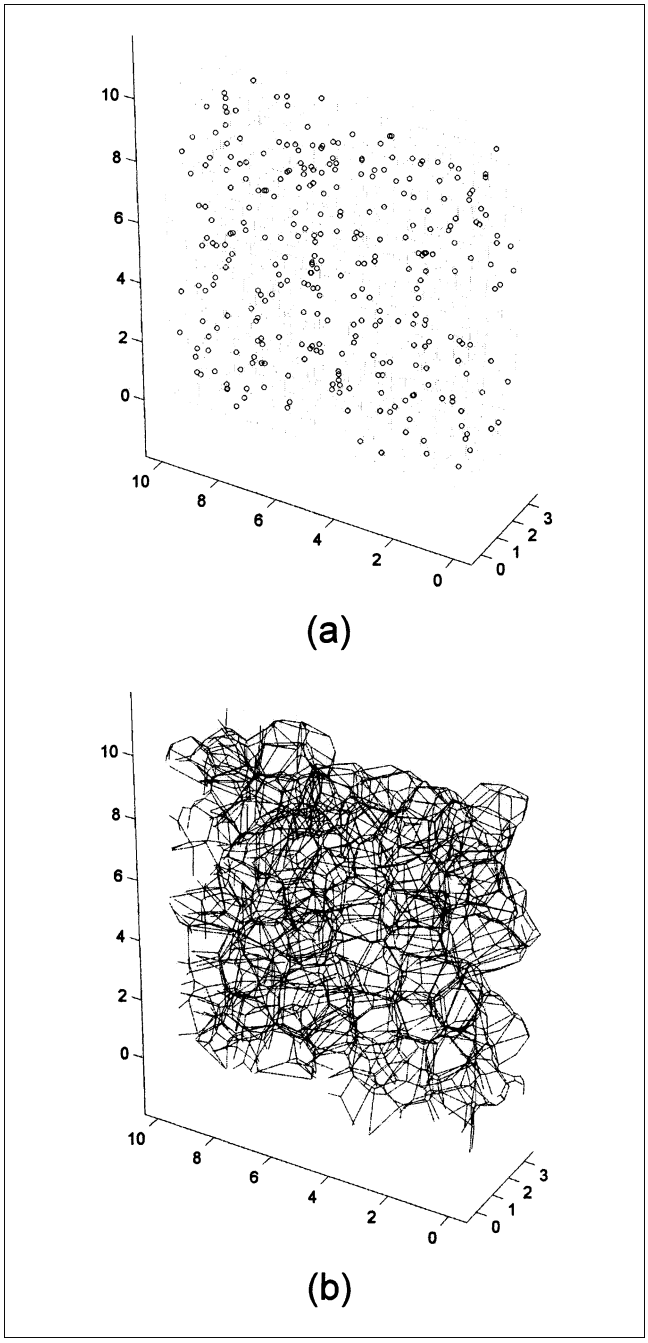

Figure 1. (a) Random base points in a 3-D domain; (b) periodic Voronoi diagram constructed around the base points.

modeling capillary-dominated transport, but permeability calculation and dynamic modeling require the fibers to have finite radii.

The Voronoi networks differ in certain ways from most real fibrous materials. The fiber segments come together in joints rather than resting upon one another. Also, each fiber segment in the model has a characteristic length similar to the pore size, whereas fibers in real materials are often longer. Intuitively, one might expect this latter effect to cause spatial correlations in real structures that would not appear in the Voronoi networks.

These differences notwithstanding, the Voronoi diagrams are a powerful tool for generating fibrous structures. The most important attribute of this approach is that by choosing the placement of the initial base points, remarkably varied pore structures can be created. This variation occurs because the base points dictate the final pore locations, the orientation of the pores relative to one another, and ultimately the orientation of the fiber segments. Morphologic parameters that can easily be controlled by the placement of base points include pore density, uniformity of pore spacing (or lack thereof), relative orientation of the pores, and larger-scale spatial correlation or heterogeneity. In all cases, the base-point locations must contain a random component (which can have a very small contribution), to prevent degeneracy problems when constructing the network.

Figure 2 contains images of six different fibrous materials generated as described earlier. The view is through the thin direction of the networks (five to six pore diameters perpendicular to the page). Networks that are thin in one direction can be used to represent thin fibrous mats (such as paper, fibrous membranes, and so on), as shown in later examples. Each material has a distinct structure, influenced only by the manner in which the initial base points were laid down. After the network is created, the characteristic pore spacing and fiber radii are assigned, which in turn dictates the porosity, interconnectivity, and permeability. Although these networks do not represent a specific type of material, they are physically representative network models in the sense that flow modeling is performed in a completely defined, three-dimensional structure that has no adjustable parameters associated with the geometry. (For instance, porosity cannot be scaled independently of pore-to-pore distances or of permeability.) Other parameters such as wettability and initial saturation are associated with the flow model rather than the network itself.

An additional parameter that is very important in fibrous materials is anisotropy, which is caused by the fiber particles having a preferred orientation. While this factor is difficult to introduce using the base-point assignments, it can be easily introduced once the Voronoi diagram has been created by stretching or compressing the network anisotropically. (Numerically, this procedure consists of nothing more than scaling all x coordinates, for instance, by some constant factor while leaving the y and z coordinates fixed.) An example of transport in an anisotropic material is given later.

Generating a periodic, three-dimensional Voronoi diagram is not a trivial exercise. In this work, a Delaunay tessellation is used as an intermediary; each Delaunay cell is defined by a circumsphere on which four base points lie and which encloses no other base point. For a nondegenerate set of base points, the Delaunay tessellation is unique. It is the geometric dual of the Voronoi diagram, so the latter network is easily created by joining centers of the circumspheres through all faces of the Delaunay tetrahedrons. (This somewhat indirect approach for generating the Voronoi networks was employed mainly to make use of already-existing tessellation codes.)

Parameters calculated from pore and network structure

Numerous parameters associated with the network are required for flow simulation. Those parameters that are related only to pore structure (as opposed to dynamic, physiochemical, or fluid properties) can be calculated directly once the network is created. Table 1 is a list of the geometric parameters used in this model. Each pore in the network can have any number of throats emanating from it, and the geometric parameters are associated with either a pore or a pore throat, as indicated.

The overall domain dimensions are specified from the outset, and the pore locations correspond to the base point positions within the domain. Hence, these parameters are defined before the Voronoi diagram is constructed.

The volume of each pore must be known for two reasons. First, the porosity of the network is calculated by dividing the total void volume by the total domain volume. Second, this parameter is used in many types flow computations (such as fluid-residence-time calculations for solute transport and phase-saturation calculations for multiphase flow). Determining a pore's void volume is a two-step process: calculation of the total polyhedron volume associated with the pore, followed by subtraction of the fiber volume within the polyhedron. The total polyhedron volume is a straightforward geometric calculation once the structure of the Voronoi diagram is known. The fiber volume calculation, however, is more involved. The part of a fiber segment that lies inside one polyhedron is a wedge, defined by the interior angle where two polyhedron faces meet. The ends of these wedges are cut at various angles relative to a fiber-segment's axis, depending on the geometry of the intersection with other fibers. The volume of each wedge is calculated using an analytic volume integral, and all wedges within a polyhedron are summed-up and subtracted from the total polyhedron volume to find that pore's void volume.

The radius of the largest inscribed sphere is required for multiphase calculations. It defines the maximum radius of a stable fluid–fluid interface that can exist in a pore. This maximum radius, in turn, dictates the minimum local capillary pressure when two fluids exist in that pore. Because pores in the fiber network are cagelike, the largest enclosed sphere will bulge out of the pore on some of its faces. (Picture a cube made of straws, and a balloon blown up in its center. At its largest diameter, the balloon would bulge out all six sides of the cube to some degree, depending on the radii of the straws.) The diameter of this bulging sphere is calculated using a simplex search, where the search is used to determine the central point in the pore that maximizes the smallest distance from the central point to a fiber segment.

Interconnectivity is implicit in the Voronoi structure. It is stored as a series of integer values assigned to each pore; these values denote the set of neighbors that can be accessed through the various pore throats emanating from that pore.

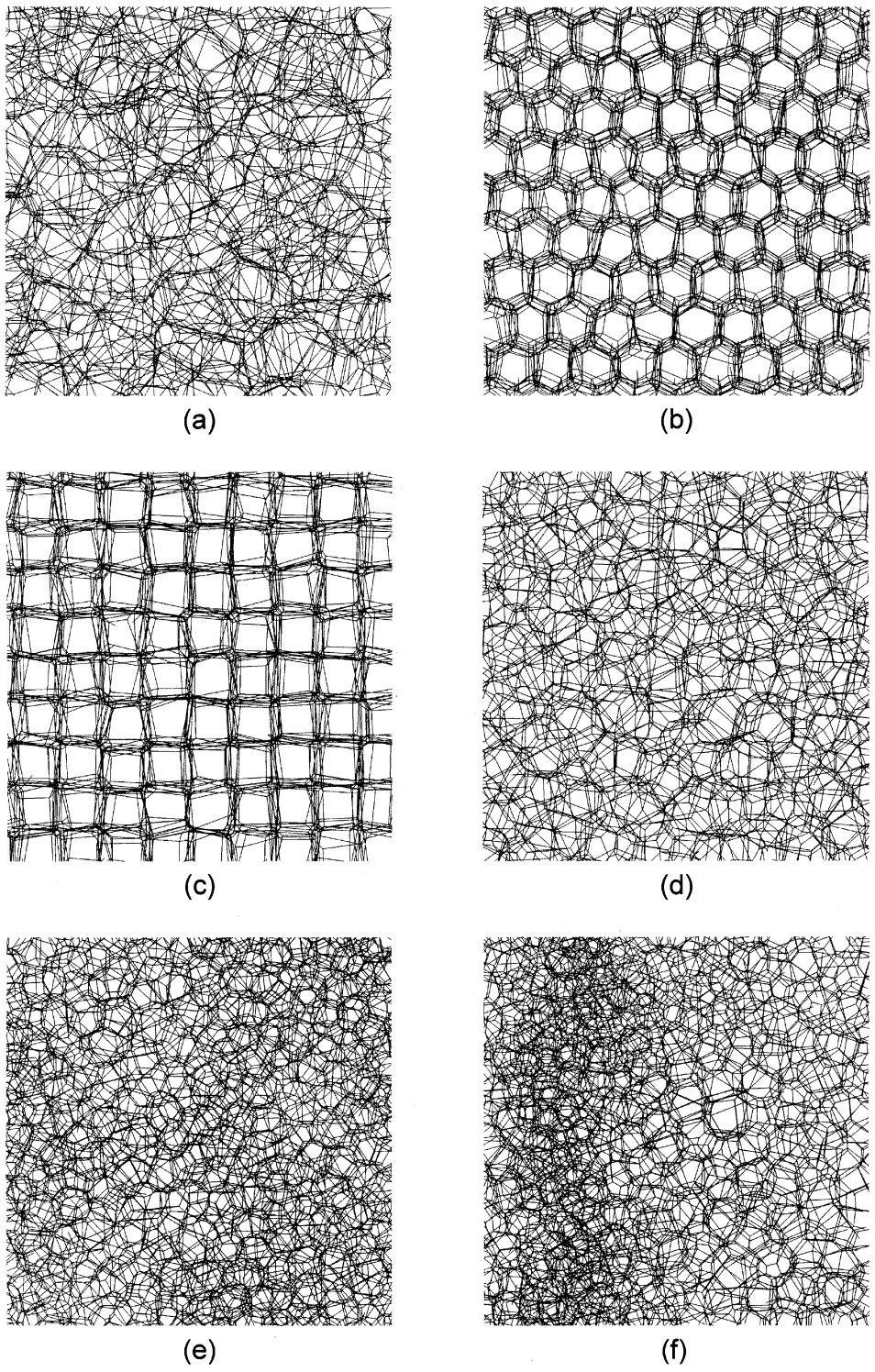

Figure 2. Prototype fiber networks viewed through a thin direction: (a) random; (b) semiordered (orthorhombic); (c) semiordered (cubic); (d) random but macroscopically uniform; (e) random with spatial correlation; (f) heterogeneous.

Additionally, since the domain is periodic, each neighbor is assigned an integer vector, indicating whether the neighbor pore is located in the primary domain or in one of the 26 periodic domains surrounding the primary domain. Because the coordination number varies widely for these networks, compact storage is used for the interconnectivity data and all

Table 1. Network Parameters for Fluid-Flow Modeling

Parameter Description	Association	Type
Overall domain dimensions	Network	Scalars
Location of each pore	Pore	Vector
Void volume of each pore	Pore	Scalar
Radius of largest inscribed sphere in each pore	Pore	Scalar
Interconnectivity: pore no. accessed through each throat	Pore	Scalar array
periodicity direction		Vector array
Cross-sectional area of each throat	Throat	Scalar
Radius of max. inscribed circle in each pore-throat cross section	Throat	Scalar

pore-throat parameters, which significantly decreases memory requirements.

Pore throats are the shared polygon faces between Voronoi cells. The shape and size of their flow areas depend on the radii of the fibers on their perimeters. The two geometric parameters associated with pore throats are the cross-sectional area and the maximum inscribed circle. The cross-sectional area commonly is used in hydraulic conductivity calculations. The maximum inscribed circle dictates the capillary entry pressure for the nonwetting phase to invade a pore throat.

Permeability and Single-Phase Flow

Single-phase flow is modeled by treating the pore network as an interconnected pipe network (or electrical resistor network). Using the pipe-network analogy, the flow rate between two neighboring pores i and j is written as $q_{ij} = (G_{ij}/\mu)(P_j - P_i)$, where G_{ij} is the hydraulic conductivity of the bond joining the two nodes. For constant-density fluids, the mass-conservation equation for an interior pore is

$$q = 0 = \sum_{j=1}^{n} \frac{G_{ij}}{\mu}\left(P_j - P_i\right) \tag{1}$$

where n is the number of neighbors of pore i. Writing Eq. 1 for all pores in the network and expanding the summation gives a sparse set of linear equations. One of two types of boundary conditions can be used. The first option is to specify pressure at opposing ends of the network. This approach means that certain p_j terms in the mass balances are known (that is, where a pore connects to the inlet or outlet), thus generating righthand-side terms in the matrix equation. The second option is to specify the net volumetric flow rate, along with pressure on one flow face of the network. Using the second option, an additional equation constraining the sum of flow rates into all inlet pores (or outlet pores) to a specified value is written as

$$Q_{\text{in}} = \sum_{\substack{\text{inlet}\\ \text{pores}}} \frac{G_{ij}}{\mu}\left(P_j - P_i\right)\Big|_{j\,=\,\text{inlet throat}} \tag{2}$$

Equation 2 adds one equation to the system as well as one unknown, the inlet pressure P_j.

In high SVF materials such as consolidated rocks or even packed beds, pore throats are viewed as capillary tubes in the network approximation. A Poiseuille-type calculation can then be used to estimate hydraulic conductivity (usually with some correction for cross-sectional shape and/or converging diverging geometry along the axis). However, this strategy is problematic for the fibrous materials discussed in this article because of the very large range of possible SVF. At low SVF, the Poiseuille-flow calculations are expected to be less appropriate for approximating viscous drag. These issues are examined below, where drag calculations are made using the standard approach, followed by an alternative approach.

High solid volume fractions

In the prototype networks, SVF is controlled by altering the diameter of fiber segments. As the diameter increases, the throat cross sections become smaller and the throats become longer along the flow axis. Hence, at least in a limiting sense, the pore throats assume a ductlike geometry. They also have a converging–diverging character, because flow through the duct is transverse with respect to bounding fibers.

The hydraulic conductivity of these ductlike geometries is calculated using an effective radius as defined by Bryant et al. (1993a). Specifically, the effective radius is calculated as the arithmetic mean of r_c and r_e, the radii of the largest inscribed circle and the radius of the equivalent circle based on cross-sectional area. The effective radius is then used in the Hagen–Poiseuille equation to define the hydraulic conductivity of the throat, with the duct length set equal to the fiber diameter since it defines the distance along the duct axis. Finally, a correction is made to the hydraulic conductivity to account for its converging–diverging geometry using the method described by Thompson and Fogler (1997).

Once all throats are assigned hydraulic conductivities, the pressure in each pore is found using the system of conservation equations (Eq. 1), after which the flow through any given pore throat can be calculated using $q_{ij} = (G_{ij}/\mu)(P_j - P_i)$. Depending on the boundary conditions used, solution of the system of equations also gives the total flow rate through the network (if boundary pressures were defined), or the pressure drop across the network (if the flow rate was imposed). In either case, permeability can be found by rearranging the one-dimensional form of Darcy's law to give

$$K = \frac{Q}{A}\frac{\mu}{(\Delta P/L)}, \tag{3}$$

where A and L are dimensional quantities defined by the domain shape. Because periodicity was employed when creating the Voronoi network, these two values are exact even for disordered materials. If the material is anisotropic, the permeability tensor can be defined by repeating the single-phase flow calculation in the other two coordinate directions.

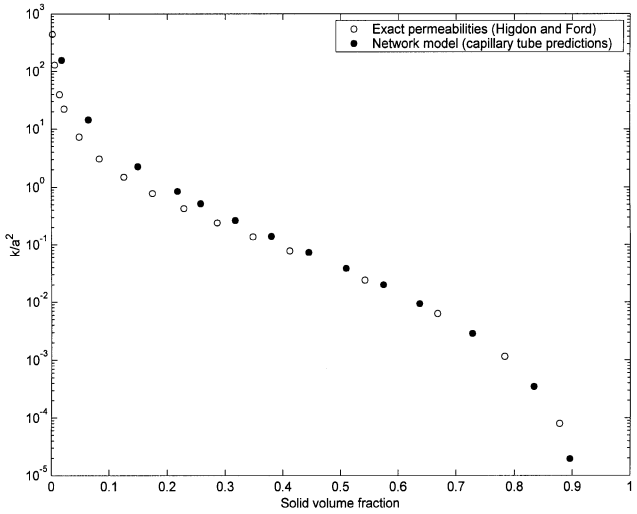

Figure 3. Network-model permeability predictions using conventional hydraulic-conductivity calculations.

Rigorous comparison of experimental vs. computed permeabilities is generally not possible, since our main interest is in disordered materials and since the networks are derived from prototype materials. However, a rigorous comparison of cubic-fiber permeabilities can be made using exact values from Higdon and Ford (1996). Using the Voronoi technique, cubic lattices were generated by placing base points inside a simple cubic grid. Permeabilities were found for a wide range of SVF, and then were nondimensionalized using the fiber radius. The results of these calculations are shown in Figure 3 along with exact permeability values from Higdon and Ford (1996). The agreement is excellent for $0.6 < \phi < 0.8$. At very high densities ($\phi > 0.9$), the network model underpredicts permeability by about 50%. At $\phi \approx 0.5$, the network model overpredicts permeability by about 20%. And, at low volume fractions, the network model is in error by about a factor of 3.

Low solid volume fractions

At low SVF, a fluid particle is surrounded by more of a cagelike than tunnel-like geometry. Consequently, the capillary tube assumption (which implies a strong orientation effect and axial pressure gradient) is not an accurate picture of the local flow. Instead, streamlines are probably oriented with the macroscopic pressure gradient more so than with the local geometry. This argument raises concerns about how one quantifies the contribution to pressure drop from the fibers. The approach described below reflects these issues, but also reflects the need to maintain the general network-model framework that is implicit in Eq. 1.

The approach is borrowed from Jackson and James (1982), who developed a simple model for the permeability of random fibers. They used asymptotic expressions for Stokes drag across and along parallel cylinders arranged on a square lattice. In a dimensional form, these expressions are usually written in terms of two parameters, the cylinder diameter and the lattice spacing. Jackson and James nondimensionalized the equations using the cylinder diameter, and then rearranged them to give permeability as a function of the SVF. They then argued that the permeability of a cubic cylinder lattice is the additive drag from parallel and perpendicular segments, with a two-thirds weight for transverse flow and one-third weight parallel flow, and further, that the resulting permeabilities should be reasonable estimates of random-fiber permeabilities. Their model was updated in a later article (Jackson and James, 1986), to include more complete asymptotic expressions and shown to compare favorably with experimental permeabilities.

A similar technique is used here, except it is applied locally rather than in an average sense. Specifically, a local porosity is defined by analyzing the fiber geometry near the pore throat of interest. This porosity is then used in the asymptotic expressions for drag due to flow through cylindrical arrays. The expressions (taken from Jackson and James, 1986), are as follows

$$\frac{k}{a^2} = \frac{1}{4\phi}\left[-\ln\phi - 1.476 + 2\phi - \frac{\phi^2}{2} + O(\phi^4)\right] \quad (4)$$

for flow parallel to a square array (attributed to Drummond and Tahir, 1984), and

$$\frac{k}{a^2} = \frac{1}{8\phi}\left[-\ln\phi - 1.476 + 2\phi - 1.774\phi^2 + 4.076\phi^3 + O(\phi^4)\right] \quad (5)$$

for flow transverse to a square array (attributed to Sangani and Acrivos, 1982).

Following Jackson and James's method, a permeability is defined by weighting contributions from flow along fibers and is normal to fibers. In contrast to their model, however, this permeability is assumed to represent a *local* conductivity to flow, and the value is transformed to give the numerical hydraulic conductivity for a pore throat. In this way, the network model allows contributions from the fiber drag to be distributed nonuniformly, which is the basic intent of a pore-level approach. Clearly, the methodology is not rigorous for a number of reasons. The calculation of a local porosity (defined on a throat-by-throat basis) is somewhat ambiguous. The use of square lattices for the drag calculations is arbitrary since the materials of interest are disordered. And, the weighted addition of normal and parallel drag contributions is not a precise representation of the drag contribution from fibers that join together in random orientations. Despite these concerns, the level of rigor included in these steps is commensurate with the network modeling framework as a whole, and indeed the obvious alternatives would be much more complex and computationally intensive.

As with the standard hydraulic conductivity calculations, permeability comparisons were made for cubic networks and are shown in Figure 4. In this case, the agreement is excellent at low volume fractions: less than 10% error for $\phi < 0.3$. At around $\phi = 0.6$, there is dramatic divergence of the estimated permeabilities for both $O(\phi^2)$ and $O(\phi^3)$ expansions, which is to be expected because the calculated results are far from the low-ϕ asymptotic limit for which Eqs. 4 and 5 are valid.

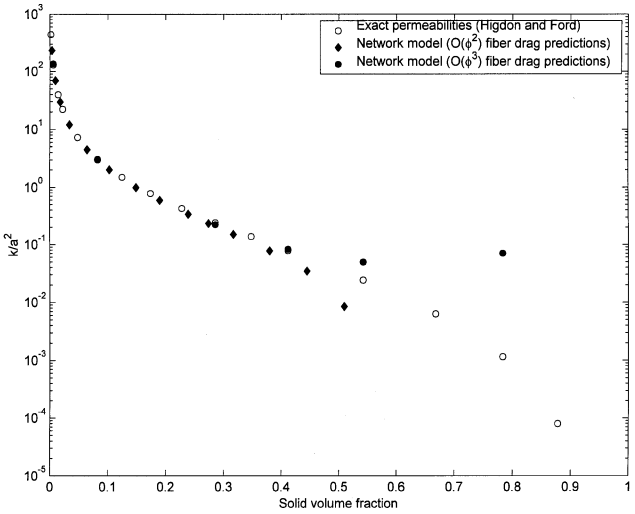

Figure 4. Network-model permeability predictions using modified hydraulic-conductivity calculations.

Permeability results for general cases

The two approaches for calculating hydraulic conductivity are fairly complementary with regard to the ranges over which permeability calculations are accurate. Hence, to model materials of arbitrary SVF, the more appropriate method is chosen on a throat-by-throat basis. Since neither method shows excellent accuracy over the middle range, a weighted average of two hydraulic conductivities is used for pore throats in the range $0.35 < \phi < 0.45$. A linear sliding scale is used to weight the two methods in this range (which prevents discontinuities in local conductivity, as pore geometry is varied). Also, since the capillary-tube approach overestimates hydraulic conductivities, the $O(\phi^2)$ expression for transverse flow was used because it underestimates hydraulic conductivity in this range.

Table 2 contains permeability predictions for cubic lattices using this integrated approach for calculating hydraulic conductivities. The error is less than 10% over significant fractions of the permeability range, but higher than 10% in the middle range and at the extreme low end. We view these results as excellent in the general framework of network modeling, especially considering that no adjustable parameters were used, and that both the solid volume fraction and permeability span orders of magnitude.

The more interesting problem is modeling fluid flow in random materials, for which some general comparisons are possible. Random networks were created (see Figure 2a), which means base points were placed randomly in a domain prior to generating the Voronoi network. Table 3 contains permeability predictions for cube-shaped domains of various size and volume fraction. Network size is controlled by adjusting the number of points placed in the domain; since the permeabilities are given in a nondimensional form, the dimensional domain size is immaterial for these results. Solid volume fraction is controlled by adjusting the fiber diameter. In Table 3, fiber diameters are given in a dimensionless form, scaled by the average pore spacing.

Table 2. Quantitative Permeability Predictions for Cubic Lattices

Solid Vol. Fraction	k/a^2 (Network Model)	k/a^2 (Higdon & Ford)	% Error
0.00571	134.7	128.4	4.91
0.0221	22.32	22.09	1.04
0.0829	2.950	3.059	−3.56
0.228	0.3918	0.4263	−8.09
0.348	0.1302	0.1327	−1.88
0.412	9.630×10^{-2}	7.818×10^{-2}	23.2
0.543	2.904×10^{-2}	2.414×10^{-2}	20.3
0.669	6.423×10^{-3}	6.329×10^{-3}	1.48
0.784	1.111×10^{-3}	1.151×10^{-3}	−3.48
0.914	3.397×10^{-6}	6.283×10^{-6}	−45.9

The random fibers have higher average permeabilities than cubic lattices of the same volume fraction, the difference being more significant at high and low SVF (~15% larger at $\phi = 0.084$ and ~25% larger at $\phi = 0.665$, while only about 5% greater at $\phi = 0.41$). The difference at high SVF is not surprising because the effects of a few large pores in the random lattice can contribute significantly to the overall permeability.

Networks of 512 pores (8 characteristic pore-to-pore distances per side of the cubic domain) appear to be large enough to give size-independent permeabilities although, somewhat surprisingly, the standard deviation in permeability is larger for the 1,000-pore networks. Networks having moderate SVF appear to be more uniform in a couple of ways. As stated earlier, permeabilities are closer to the values for a uniform cubic lattice. Also, the standard deviation in permeability is significantly smaller than for the high-ϕ and low-ϕ cases. The $\phi = 0.548$ networks became nonconductive with increasing size, suggesting that for the random Voronoi networks, only finite-size percolation clusters exist at this volume fraction.

Figure 5 shows permeability, predictions over a very large range of SVF as compared to the experimental results collected by Jackson and James (1986). Each triangular data point is generated from a statistically independent 512-pore random network. The simulated results quantitatively follow the trend of the experimental data. This agreement is not

Table 3. Permeability and Standard Deviation in Permeability of Random Networks as a Function of Solid Volume Fraction and Network Size

	Dimensionless Fiber Diameter = 0.148			Dimensionless Fiber Diameter = 0.378			Dimensionless Fiber Diameter = 0.548		
No. Pores	No. Networks	Solid Vol. Fraction	Permeability (k/a^2)	No. Networks	Solid Vol. Fraction	Permeability (k/a^2)	No. Networks	Solid Vol. Fraction	Permeability (k/a^2)
64	10/10	0.0845 ± 0.0013	3.026 ± 0.428	10/10	0.4115 ± 0.0038	$(0.887\pm0.171)\times10^{-1}$	9/10	0.6655 ± 0.0034	$(5.823\pm1.658)\times10^{-3}$
216	10/10	0.0841 ± 0.0006	3.311 ± 0.176	10/10	0.4093 ± 0.0027	$(1.003\pm0.060)\times10^{-1}$	7/10	0.6650 ± 0.0043	$(8.857\pm0.727)\times10^{-3}$
512	10/10	0.0842 ± 0.0004	3.388 ± 0.107	10/10	0.4102 ± 0.0020	$(1.006\pm0.044)\times10^{-1}$	7/10	0.6652 ± 0.0037	$(8.239\pm0.602)\times10^{-3}$
1,000	10/10	0.0841 ± 0.0002	3.377 ± 0.129	10/10	0.4107 ± 0.0012	$(1.007\pm0.065)\times10^{-1}$	3/10	0.6648 ± 0.0026	$(7.737\pm0.680)\times10^{-3}$
1,728	10/10	0.0842 ± 0.0002	3.523 ± 0.066	10/10	0.4106 ± 0.0010	$(1.077\pm0.030)\times10^{-1}$	0/10	0.6653 ± 0.0011	

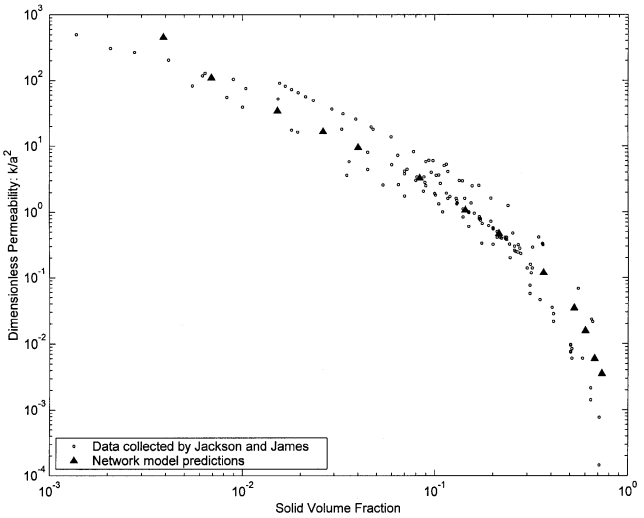

Figure 5. Permeability of statistically independent random networks plotted with experimental results collected by Jackson and James (1986).

surprising at lower SVF because the simple model of Jackson and James also predicted the general trend well, but the current model extends the range of volume fractions significantly across all values found in practice.

The more important distinction between the network approach and averaged results is that the network approach allows one to explicitly examine effects associated with disorder and heterogeneity. According to Figure 5, experimentally measured nondimensional permeabilities vary by an order of magnitude at any one volume fraction. To quantify how the random component contributes to this spread, error bars were added to the Figure-5 plot using (three times) the standard deviations from Table 3. The error bars were essentially the size of the triangular markers themselves (which is why they were left off). This observation indicates that the local randomness in pore orientation and pore throat size captured by the Voronoi networks is a relatively small contributor to the permeability variation in real materials. Numerous other reasons exist for permeability variation, including long-range spatial correlation, differences in the fibers themselves (for example, flexibility, curvature, roughness), inertial effects, or experimental error. Jackson and James (1986) discuss some specific observations about the materials used in their collected data set, and in this way they define a more uniform subset of data than that used in Figure 5.

Multiphase Flow: Pore-Scale Constitutive Relationships

In addition to the network and geometric parameters listed in Table 1, at least two constitutive relationships are required for dynamic modeling of multiphase flow. The first is the capillary pressure vs. saturation relationship for each pore. The second is the pore-throat hydraulic conductivity to each phase, which is also assumed to be a function of local saturation. Although both of these parameters depend strongly on the pore-scale configuration of the phases, the complexity of the pore structures and interface shapes precludes making rigorous calculation of their values. Hence, numerous simplifications are required.

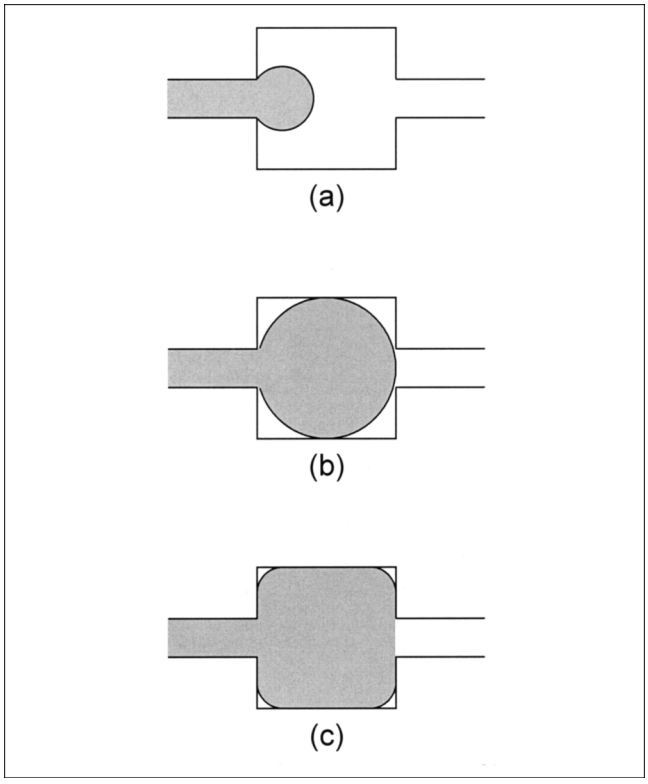

Figure 6. Wetting-phase configurations in an idealized pore.

Local capillary pressure

A capillary pressure difference between the wetting and nonwetting phases is observed in multiphase phenomena in porous media, due to the curvature of the interfaces within the pore space combined with interfacial tension between the fluids. Average capillary pressure curves are commonly generated for use in continuum modeling. In a network model, however, the capillary pressure can be resolved at the pore scale as a function of the interface shape in a given pore. For simplicity, one typically assumes that the interface takes on an equilibrium configuration. Thus, the local capillary pressure can be determined using the Laplace equation ($P_c = 2\sigma \cdot \cos\theta/r$). Ultimately, it becomes a function of the pore geometry and phase saturation, providing an important coupling between the two fluid phases in the dynamic algorithm discussed below.

Unlike the macroscopic capillary pressure relationship, which is monotonic with saturation, capillary pressure in a pore passes through a minimum. The reason for this behavior is illustrated in Figure 6, which depicts a nonwetting phase (gray) entering a single pore with inlet and outlet throats. As the nonwetting phase enters the pore (Figure 6a), the capillary pressure is high due to the interface having to squeeze through the small adjoining throat. A minimum capillary pressure occurs when the interface reaches a maximum cur-

vature (Figure 6b). To further reduce the wetting-phase saturation, the interface must squeeze into corners, requiring the capillary pressure to increase (Figure 6c). Interface configurations like the one suggested by Figure 6a are transient: depending on the detailed dynamics, the interface can retract back into the pore throat, jump quickly to a stable configuration, or snap off so that the nonwetting phase becomes disconnected. Although much is known about interface motion, the complexity requires that these dynamics be modeled quite simplistically in network models. In this model, we allow only retraction or advance of the interface once it has begun to enter a pore throat, depending on the behavior of the local pressure fields in subsequent time steps.

The main challenge in generating a local capillary pressure function is evaluating the equilibrium shape (that is, curvature) that an interface will assume in an arbitrary-shaped pore at any given phase saturation. A common approach for lattice-based models is to use simple pore and pore-throat shapes that allow for the use of analytic solutions for interface geometries (Dillard and Blunt, 2000). The interface geometry usually cannot be determined exactly for more complex geometries, so approximate solutions are used. The capillary pressure function used in this model is defined in the following way.

(1) The minimum capillary pressure for a given pore is calculated by substituting the radius of the maximum inscribed sphere (see Table 1 and its discussion) into the Laplace equation. The corresponding wetting-phase saturation, $S_{\max}$, is found by subtracting the nonwetting-phase volume in the pore from the total volume of the pore (and nondimensionalizing). The nonwetting-phase volume is assumed to equal the volume of the largest inscribed sphere minus the volume of any parts that bulge out of the pore.

(2) The capillary pressure vs. saturation in the range $S > S_{\max}$ is calculated as follows (note $S_{\max}$ corresponds to the highest *stable* wetting phase saturation). First, as the inscribed sphere shrinks from its maximum radius, its volume and radii are used to generate saturation and capillary pressure values, respectively. When the radius of the sphere is equal to the radius of the largest connecting pore throat, the capillary pressure function then becomes constant between that saturation value and $S = 1$. The main reason for this plateau is numerical stability, but it also reflects a reasonable view of the actual physics.

(3) In the range $S_{\max} > S > 0$, saturation is allowed to decrease to zero, with a corresponding increase to an infinite capillary pressure. To generate a functional relationship, an expression was obtained using a cube-shaped pore (in which wetting films are squeezed into the eight corners of the cube and along the 12 edges of the cube as the capillary pressure increases). The resulting function is mapped onto the range $S = [0, S_{\max}]$ on a pore-by-pore basis.

The low-saturation behavior (that is, item 3 above) represents a significant simplification of the expected interface behavior. This approach was taken mainly to avoid making the solid-volume calculations that would otherwise be required (an approach that borders on the intractable in the current model). However, we do note that even this simplistic technique allows for significant variability from one pore to another because both $S_{\max}$ and the plateau capillary pressure vary widely. Figure 7 serves to illustrate this variability with a couple of examples of local capillary pressure curves.

Finally, we note that an important area of current research is the numerical predictions of interface behavior in a real porous media, primarily for applications involving interfacial dissolution (for example, Bryant et al., 2000). Hence, the methodology for making local capillary-pressure calculations should improve as these new techniques are developed.

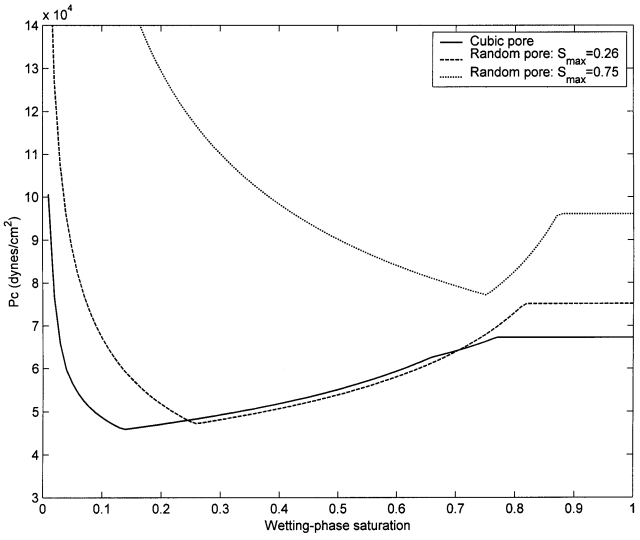

Figure 7. Examples of local air–water capillary pressure vs. saturation functions used in the network model: solid volume fraction ≈ 0.04; average pore size ≈ 0.5 mm.

Phase hydraulic conductivities

Hydraulic conductivities of the individual phases are functions of saturation (and ultimately capillary pressure), as shown in Figure 8 for an idealized throat of square cross section. The difficulties in calculating these values are similar to the problems discussed in the previous section. Specifically, the geometries of the wetting films are not known exactly, and even if they were, rigorous calculation of the fluid flow (to obtain hydraulic conductivities) is a difficult numerical problem.

A rigorous pore-scale analysis of wetting-film conductivity was made by Ransohoff and Radke (1988) for specific geometries. They performed finite-element computations to determine conductivities for various parallel corner flows (which despite requiring rather involved computations, remain simplistic models of real porous media film flows). Their results have been used repeatedly in network modeling studies. The following approach is used in this work.

(1) For a given pore throat, the area of the largest inscribed circle along with the throat's cross-sectional area are used to generate a polygon with an equivalent ratio of these two areas. For $A_{insc}/A_{c.s.} \leq 0.6046$, the equivalent shape is a regular polygon. For ratios smaller than this limit, an isosceles triangle is used.

(2) From the equivalent polygon, the corners, half angles, α, are computed [see Ransohoff and Radke (1988) for a definition of α]. In this approach, regular polygons will have only

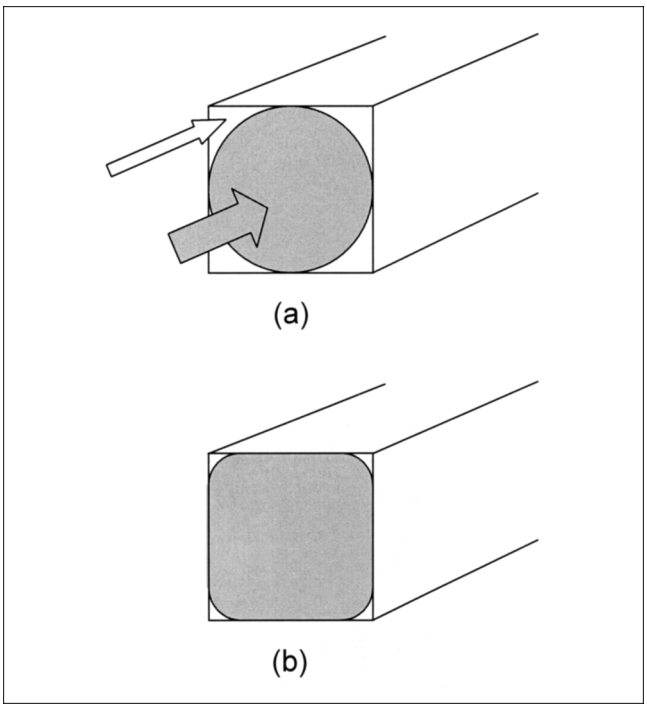

Figure 8. Effect of capillary pressure on the phase hydraulic conductivities.

one value of α, while the isosceles triangles will have two values of α.

(3) The radius of curvature of the interface, a, is calculated based on the current capillary pressure in the pore. For the explicit formulation described below, "current" capillary pressures are values from the previous time step.

(4) Using α and a, the cross-sectional area of each wetting film in the equivalent polygon is found, which in turn is used to determine idealized Poiseuille hydraulic conductivities, $G_{\text{Poiseuille}}$.

(5) Ransohoff and Radke's results are used to calculate the dimensionless flow resistance, β. Since β values are given in tabulated form only, an interpolating function was fit to the first row of Table II from their article (no stress boundary conditions at the interface), and then used in the network model. The flow conductivity for a single corner film is $G_{\text{corner}} = G_{\text{Poiseuille}}(8/\beta)$.

(6) The dimensionless wetting-phase hydraulic conductivities are the sum of all corner conductivities in a throat, nondimensionalized with the absolute conductivity of that throat: $g_w = \sum_{\text{corners}} G_{\text{corner}}/G_{ij}$.

(7) The nonwetting-phase hydraulic conductivity is calculated as $g_{nw} = 1 - g_w$. This relation is not fundamentally true. However, because the film conductivities are generally small, this approximation ensures that the nonwetting-phase conductivity approaches the total conductivity of a throat, which can be justified using qualitative arguments and/or relative permeability data.

A couple of comments should be made. First, the throat angles could be defined directly from the fiber network rather than from an analysis of the areas if this were perceived to be more accurate. Due to the level of approximation already in place, we feel this distinction is minor. The advantage of using the equivalent polygons is that it allows the multiphase flow algorithm to run with a compact set of parameters (that is, Table 1), rather than a full morphologic description of the fiber. Second, even if the wetting-film conductivity of a throat could be determined very accurately, significant questions remain about whether the films are sufficiently well connected to provide fluid transport. We suspect that for fibrous materials the overall film connectivity is poor, but this issue requires further research.

Multiphase Flow Algorithms

Despite the practical importance of permeability prediction, modeling is more useful for multiphase flow problems. Relevant applications include drying (such as in pulp processing), wicking flows (such as the performance of adsorbent fibers), and other fluid injection processes (such as impregnation of fibers to manufacture composite materials).

The differences between modeling multiphase flow and single-phase flow are enormous. In addition to the fluid displacements shown here being transient by definition, multiphase processes are more sensitive to pore-scale structure, and they depend strongly on surface chemistry because of the interfacial effects.

Two algorithms are presented here. The first is a quasi-static algorithm, which is conceptually simple and very efficient computationally. It neglects viscous effects, however. The second is a type of dynamic algorithm, which accounts for all relevant physics. The trade-off is a large increase in complexity as well as computational requirements.

Quasi-static displacement algorithm

The quasi-static assumption requires that all viscous effects be negligible. It is difficult to set a definitive criteria under which this assumption can be justified. Most often, the capillary number ($Ca = \mu v/\sigma$) is used, although this form does not provide for universal scaling (Dullien, 1992, p. 454). The most significant consequence of quasi-static modeling is that, without viscosity, a characteristic time scale cannot be found. Without a time scale, it is not possible to model dynamic behavior such as spontaneous imbibition, viscous fingering, and displacement times. Despite this severe limitation, quasi-static simulations are useful in the appropriate contexts. One example is the modeling of capillary pressure curves, which are intended to be a probe of pore structure and should be free from viscous effects. A second example is the use of network modeling for certain subsurface flow problems where viscous forces govern large-scale behavior, but interfacial forces govern pore-scale behavior.

For quasi-static displacement by the nonwetting phase, the displacement pattern depends only on pore-throat geometry and the network interconnectivity; hence, the displacement algorithm is largely a matter of bookkeeping. It begins with a known saturation distribution from which possible locations that the interface can advance are found. More often than not, the initial condition is a medium saturated with the wetting phase, and the possible locations for the interface to advance from are the inlet pore throats. During each step of the quasi-static displacement, a search is performed over all interface positions to determine the minimum capillary pres-

sure that will allow the nonwetting phase to advance. After increasing the capillary pressure to this critical value, the nonwetting phase invades the connecting pore and any subsequent pore-throat-to-pore combinations that can be accessed at the new capillary pressure. Once no further invasion can occur, the applied capillary pressure is increased by the next minimum increment.

A couple of logistical issues must be included in the algorithm. First, the nonwetting phase is not allowed to penetrate the outlet of the network because a complete breakthrough would prevent further invasion from occurring. (An analogous restriction can be employed during an experiment by placing a low-permeability, wetting medium at the outlet of a sample.) Second, after all the pores have been invaded, the algorithm continues to increase the nonwetting phase pressure until a specified saturation is reached. During this time, the local saturations decrease as dictated by the local capillary-pressure vs. saturation functions. Finally, in cases where gravity is included, local capillary pressures must include a contribution from a hydrostatic head, which affects the displacement process if a difference in fluid densities exists.

Quasistatic displacement by the wetting-phase differs only slightly from the previously considered case. Most importantly, the displacement pattern depends only on *pore* geometry and network interconnectivity. The initial condition must be a positive capillary pressure, and sequential reductions in the applied pressure to the nonwetting phase allow the wetting phase to invade. The reason that pore geometry governs the process is that the wetting phase invades a pore as soon as the capillary pressure drops below a critical value, at which the interface can no longer assume a stable configuration. From a simplistic point of view, the smallest pores are invaded first although this, of course, depends on interconnectivity. Logistics are important for this part of the algorithm, too. In this model, if the beginning saturation is $S_w = 0$, pores are forced to remain at zero wetting-phase saturation until they become completely invaded, even though in reality they would fill to some degree via wetting films. On the other hand, if a nonzero initial saturation is specified (for instance, at the top of a scanning curve in a capillary-pressure test), the wetting films are allowed to swell according to the current capillary pressure in the network. This latter process can cause a significant saturation increase well before the bulk wetting-phase front has moved appreciably.

In this model, neither phase is allowed to become trapped during displacement. This assumption has good physical grounds for displacement of the wetting phase because, in the quasi-static limit, the wetting phase can escape through very thin wetting films (except in media such as sphere packs, where the wetting phase can become disconnected in the form of pendular rings). The no-trapping assumption is less realistic for wetting-phase invasion because the nonwetting phase oftentimes becomes disconnected. However, it was made here for a couple of reasons. First, in the specific porous media of interest for this study, nonwetting-phase trapping has not been observed experimentally. The second reason is that the dynamic algorithm described below implicitly accounts for trapping of the nonwetting phase as well as slow drainage of wetting films. Hence, although it is much more computationally expensive, the dynamic algorithm can be used to study these features of the flow.

Dynamic displacement algorithm

Dynamic algorithms differ from quasi-static algorithms mainly in that viscous forces are accounted for by way of calculating the pressure distribution in the fluids. This difference allows rate effects to be captured, but at a considerable expense: dynamic algorithms are more difficult to develop and are orders of magnitude more computationally expensive to run. Various strategies have been proposed to capture dynamic multiphase effects (Koplik and Lasseter, 1985; Dias and Payatakes, 1986; Lenormand et al., 1988; Blunt and King, 1991; Bakke and Oren, 1996; Thompson and Fogler, 1998; Mogensen and Stenby, 1998). Because of the complexity of these algorithms, each is tailored somewhat to the specific problem that it was designed to address.

The approach employed here is a direct numerical solution of the mass conservation equations for the two fluid phases, which in essence extends Eq. 1 for the multiphase case

$$\frac{V_i}{\Delta t}\left[S_{w,i}^{l+1} - S_{w,i}^{l}\right] = \sum_j \frac{g_w^l G_{ij}}{\mu_w}\left(P_{w,j}^{l} - P_{w,i}^{l}\right) \tag{6}$$

$$\frac{V_i}{\Delta t}\left[S_{nw,i}^{l+1} - S_{nw,i}^{l}\right] = \sum_j \frac{g_{nw}^l G_{ij}}{\mu_{nw}}\left(P_{nw,j}^{l} - P_{nw,i}^{l}\right) \tag{7}$$

In these equations, S and P are saturation and pressure, respectively; the subscripts w and nw indicate the wetting and nonwetting phases; the subscript i denotes all the pores in the network, and the subscript j denotes all neighbors of pore i; the superscript l denotes the current time step and $l+1$ the next time step; G_{ij} is the hydraulic conductivity of the pore throat between pores i and j, while g_w and g_{nw} are the dimensionless, phase hydraulic conductivities discussed previously (which are defined on a throat-by-throat basis, but are not subscripted ij for clarity); V_i is the volume of each pore, μ is the viscosity; and Δt is the time step used in the discrete approximation of the original differential mass balances for each pore. The equations are nonlinear because hydraulic conductivity depends on saturation. The explicit formulation shown in Eqs. 6 and 7 is used for all results in this article (meaning that hydraulic conductivities and pressures are evaluated at the previous time step). However, the implicit formulation is also being studied to better understand numerical stability issues.

The dependent variables are related by additional algebraic equations. The phase saturations, by definition, must satisfy

$$S_{w,i} + S_{nw,i} = 1 \tag{8}$$

The phase pressures are related by the capillary pressure function described previously

$$P_{nw,i} = P_{w,i} + P_{c,i}(S_w) \tag{9}$$

Equations 6–9 are combined to give the following algebraic equation, which applies to each pore

$$\sum_j \left[\left(\frac{g_w^l G_{ij}}{\mu_w} + \frac{g_{nw}^l G_{ij}}{\mu_{nw}} \right) \left(P_{w,j}^i - P_{w,i}^l \right) + \frac{g_{nw}^l G_{ij}}{\mu_{nw}} \left(P_{c,j}^l - P_{c,i}^l \right) \right] = 0 \quad (10)$$

Equation 10 is used to generate a set of linear algebraic equations in which the wetting-phase pressures are unknown. Using the explicit formulation, hydraulic conductivities and capillary pressures are calculated using saturations from the previous time step. Since the nonwetting-phase pressure has been eliminated from this equation, all pores must contain a nonzero fraction of wetting-phase fluid for the algorithm to be stable. When modeling a "dry" material, the initial condition is set to $S_w = 0.01$ for all pores, and the algorithm is coded so that local saturations of 0.01 or less are viewed as a zero wetting-phase fraction in the hydraulic conductivity calculations.

As with the single-phase algorithm, network boundary conditions can be used to enforce either a constant injection flow rate or a constant applied pressure drop. For the constant-flow-rate case, the multiphase analogs to Eq. 2 are written

$$\sum_{\substack{\text{inlet} \\ \text{pores}}} \left[\frac{g_w^l G_{\text{inlet}}}{\mu_w} \left(P_{w,\text{inlet}}^{l+1} - P_{w,i}^{l+1} \right) \right] = Q_{w,\text{in}} \quad (11)$$

$$\sum_{\substack{\text{inlet} \\ \text{pores}}} \left[\frac{g_{nw}^l G_{\text{inlet}}}{\mu_{nw}} \left(P_{nw,\text{inlet}}^{l+1} - P_{nw,i}^{l+1} \right) \right] = Q_{nw,\text{in}} \quad (12)$$

If the only phase to be injected is the wetting phase, Eq. 11 is used alone, adding one algebraic equation and one unknown (inlet wetting-phase pressure) to the system. If the nonwetting phase is injected, both equations are required (since wetting-phase pressure is the primary dependent variable); $Q_{w,\text{in}}$ is set equal to zero, and two additional equations and unknowns are added to the system. Situations in which the injected fluid contains a nonzero fraction of each phase are currently being studied using small networks, but additional research is needed. The main issue is determination of g_w and g_{nw} in Eqs. 11 and 12, which must be subject to a *local* (history-dependent) minimum with respect to inlet pressures.

For constant-pressure boundary conditions, only one phase is allowed to flow into the network for the same reason given in the previous paragraph. If the inlet phase is wetting, $P_{w,\text{inlet}}$ is specified. If the inlet phase is nonwetting, $P_{nw,\text{inlet}}$ is specified, and Eq. 11 must also be used with $Q_{w,\text{in}} = 0$.

The resulting system has N, $N+1$, or $N+2$ equations (where N is the number of pores), depending on which set of boundary conditions is used. The equations are solved once for each time step using a preconditioned biconjugate gradient routine (Van der Vorst, 1992).

Once the pressure distribution is calculated, the phase saturations are updated by rearranging Eqs. 6 and 7 for $S_{w,i}^{l+1}$ and $S_{nw,i}^{l+1}$. The crucial aspect of this procedure is time-step selection. In explicit finite difference routines, time-step size is usually restricted by numerical stability. In this model, however, time steps are restricted by critical filling events, and Δt is necessarily smaller than stability criteria would dictate. Specifically, flow is advanced until one of the three types of critical events occurs anywhere in the network:

(1) A pore reaches the maximum stable saturation, $S_{\max}$, from either direction. Flow must be stopped at this point to prevent saturation values from jumping across the minimum in the capillary pressure function (from one high value to another high value).

(2) A pore fills with wetting-phase fluid. Clearly a time step must be stopped at this point to prevent the saturation from exceeding 1.0.

(3) A pore with a decreasing wetting-phase saturation loses one-half of the wetting-phase fluid that was present in the previous time step. The value of one-half is arbitrary. However, one must prevent large decreases in wetting-phase saturation because the corresponding changes in capillary pressure can be large, which in turn can lead to pressure oscillations.

Because a time step ends when any one of these conditions is met in any one pore, time steps are short, especially after fluid displacement has proceeded well into the network and/or for large networks. While the advantage to these limitations is that the explicit algorithm appears to be quite stable, it is very computationally intensive.

The similarity of the numerical equations to finite difference models for diffusive transport or continuum porous-media transport is apparent. However, the numerical behavior is quite different from these cases for two reasons that are related to the physics of pore-scale multiphase flow. First, during any one time step, a handful of pores (which may be widely distributed in the domain) will undergo very large saturation changes. These sudden large saturation changes cause correspondingly large changes to the coefficients in Eq. 10, and markedly changing pressure distributions from one time step to another (though perhaps small changes in the magnitudes of pressures). Conversely, in finite difference modeling, changes in coefficients usually occur slowly or are limited to a distinct region of rapid change such as a shock front. The second difference is that numerical dispersion does not occur in the network model because of the critical behavior of the phase hydraulic conductivity (that is, it is a step function of capillary pressure). This critical behavior can prevent convergence in the implicit formulation due to the hydraulic conductivity changing from "on" to "off" during iterations toward a solution for pressure.

Examples and Discussion

In this last section, a few multiphase results are presented. Although the physics of these flows are well understood qualitatively, the examples serve to illustrate how network modeling allows one to characterize fluid-flow behavior without an *a-priori* knowledge of the relevant continuum transport parameters. Effects that are normally difficult to quantify (particularly pore-scale structure), can therefore be studied.

Rate effects

The first example illustrates effects associated with the displacement rate during imbibition of the wetting phase into a dry fibrous material using the dynamic model. The general

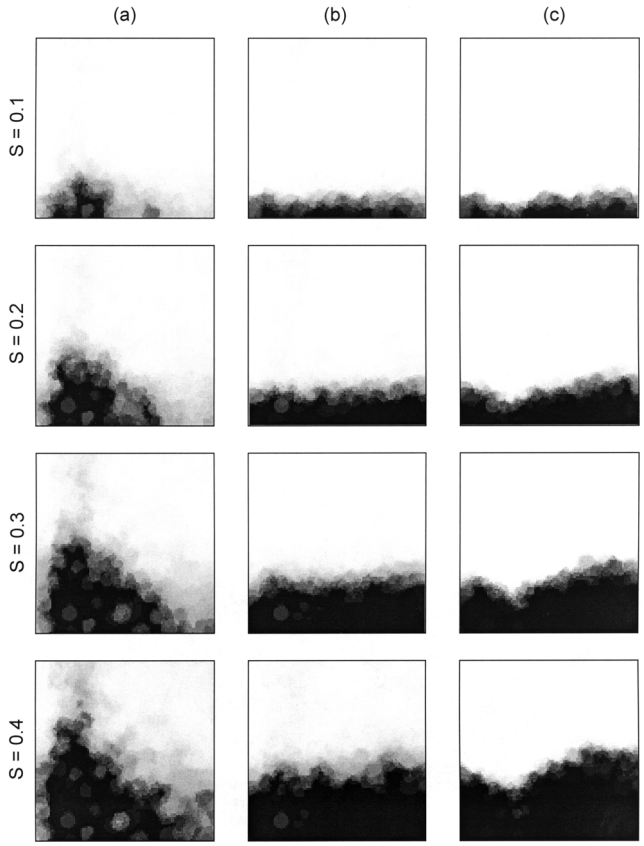

Figure 9. Imbibition of water into a dry, heterogeneous fibrous material under three conditions: (a) low flow rate ($CA_{imb} \approx 0.001$); (b) spontaneous wicking flow ($CA_{imb} = 1$); (c) high flow rate ($CA_{imb} \approx 1{,}000$).

effects of flow rate are known from previous studies (Lenormand et al., 1988). However, quantifying these effects for a specific material remains difficult, especially because the behavior is strongly coupled with morphology at both the pore scale and macroscopic scale.

Figure 9 contains three sets of images showing water invading a dry, strongly water-wet, fibrous material. The network shown in Figure 2f was used, which contains significant heterogeneity at both the pore scale and multipore scale. It is thin in the direction and perpendicular to the page (approximately six pores deep). Flow was perpendicular to the thin direction, from the bottom edge upward, against gravity. The network was scaled so that the average pore-to-pore distance was 100 μm, and a fiber diameter of 35 μm was used, which corresponded to $\phi = 0.36$. The shading in the images represents saturation averaged through the thin dimension of the networks. Hence, the images mimic what one would see by looking through a dyed fluid, or using tomography. Each of the three sets shows a sequential series of images at overall water saturations of 0.1, 0.2, 0.3, and 0.4.

Modeling imbibition is performed in one of two ways. For spontaneous imbibition, the boundary conditions $P_{inlet} = 0$ and $P_{outlet} = 0$ are imposed on the network, and the wetting-phase fluid is allowed to access all inlet pores. Alternatively, imbibition at lower or higher injection rates are modeled using a constant-flow-rate condition rather than a constant-pressure condition, which requires the use of Eq. 11.

The imbibition of water into a dry fiber is a favorable-mobility-ratio displacement. This terminology means that, because of stabilizing viscous forces, the natural tendency is for a uniform displacement front. In the current example, Figure 9b is used as a basis for comparison; it shows a natural wicking flow in which water is introduced at the bottom of the material at atmospheric pressure. The upward flow is driven by capillary forces and balanced by viscous forces behind the front. The flow rate into the fiber is highest at first, and then decreases over time as the length over which viscous forces act becomes larger. If the network were large enough, the flow would stop when the front reached a sufficient height such that the capillary pressure difference just balanced the hydraulic head of water. However, the networks are significantly smaller than what would be required to reach this limit. Using the dynamic capillary number for imbibition defined by Dullien (1992, p. 456), the case of spontaneous imbibition is assigned $CA_{imb} = 1$. (Various definitions of the capillary number are in use; CA_{imb} is a true reflection of the balance between viscous and capillary forces. For the conditions used for the Figure 9b displacements, the value of the conventional capillary number would be approximately $Ca \equiv v\mu/(\sigma \cos \theta) \approx 10^{-4} \cdot CA_{imb}$).

The displacement patterns shown in Figures 9b and 9c are high- and low-velocity displacements, corresponding to $CA_{imb} \approx 0.001$ and $CA_{imb} \approx 1{,}000$. At low capillary numbers, interfacial effects dominate the displacement, causing capillary fingering to occur. This can be seen by comparing Figure 9a to the picture of the material (Figure 2f), and noting that the dominant area of fluid transport is where the pores are smallest. At $CA_{imb} = 1{,}000$, viscous forces are dominant, and the most rapid fluid advance occurs where the pores are largest. Additionally, although the spontaneous imbibition front is the most uniform, the high-capillary-number case has the sharpest saturation front. One other important point is that even at a value of $CA_{imb} \approx 0.001$, the displacement front exhibits dramatic differences from a quasi-static simulation in the same material. To illustrate this difference, a quasi-static displacement in the same material is shown in Figure 10. It is governed nearly entirely by pore structure; gravity was included, but has a nearly negligible effect under these conditions.

It should be noted that comparison of these two cases (quasi-static vs. dynamic) must be made somewhat cautiously for a number of reasons. First, the computational algorithms are fundamentally different; for instance, the quasi-static algorithm used here does not account for capillary rise within the wetting films. Second, the dynamic algorithm becomes very slow to converge or even nonconvergent at very low capillary numbers. While these differences have prevented a direct comparison of the two methods in the $Ca \rightarrow 0$ limit, they also serve to underscore the importance of continuing research on factors, such as film dynamics in order to fully understand the limitations of the numerical algorithms. (While the microscale details of wetting films may not greatly affect the conductivity calculations, processes such as mass transfer or phase change in which the interfacial area is a dominant parameter could be affected more strongly.)

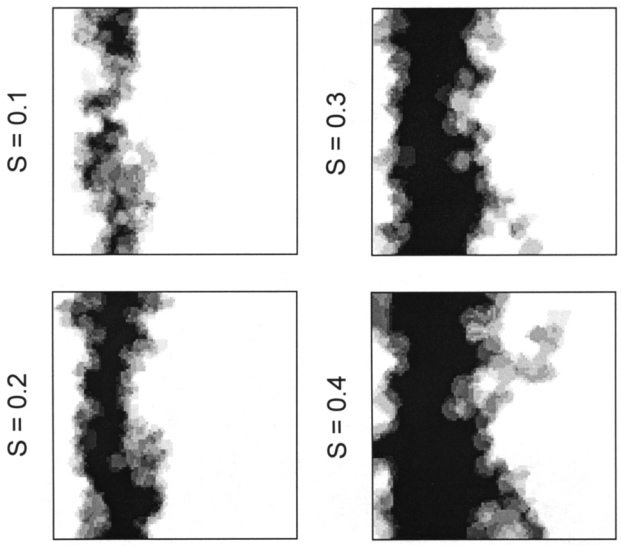

Figure 10. Quasi-static invasion of water into a dry, heterogeneous fibrous material.

Pore-scale modeling of fluid invasion into dry fibrous materials is valuable for studying processes where the fluid displacement pattern is important. For instance, during the impregnation of fibrous materials for composites materials, a uniform flow front is desirable and it is important that void formation behind the front be prevented. Notice in Figure 9a the formation of voids behind the front; the network model can be used to study the interplay between structural, surface, fluid, and dynamic properties. Ultimately, as effective numerical upscaling techniques are developed, network models will be integrated with continuum models to provide quantitative information during process design.

Morphologic effects during drop spreading

The second example illustrates the effects of pore structure and wettability on drop spreading in a fibrous material. The rapid imbibition of a liquid drop from the surface of a fibrous material is of interest in applications such as printing and the coating of fibrous materials. To emphasize the effects of structure, four types of fiber networks were generated: (1) strongly wetting with a random structure (see Figure 2a); (2) near-neutral wettability (85° contact angle) with a random structure; (3) strongly wetting with a random but highly homogeneous structure (see Figure 2d); (4) strongly wetting with a random, anisotropic structure. The first and second materials use the same random network (which was created by placing pore locations randomly in the domain), so that the effect of wettability is isolated from the structure. The third material, which is disordered but homogeneous, was created using a sphere packing as the basis for pore locations. This approach provides for random pore locations while maintaining a tight distribution of pore-to-pore distances because of the spacing imposed by the spheres in the original packing. The anisotropic network was created by compressing a random Voronoi diagram by 50% in the y-direction. Hence, the average y-component of a fiber's directional orientation equaled one-half of the x- or z-component. The networks used in these examples were created by replicating small (500-pore) periodic networks into 2,000-pore networks. They were replicated in the x- and y-directions only (that is, one small network occupied each quadrant of a x-y coordinate system). Although the structures contained repeated structure, this fact was expected to have little effect on these simulations, since the drop spreading was modeled from the center of the 2,000-pore fiber, where four different corners of the smaller, periodic domain meet.

The simulations were run under the following conditions: individual fibers were 43 μm in diameter; the networks were 450–600 μm thick; and the solid volume fraction of each network was between 0.52 and 0.53. Markings on the images show their size. The fluid droplets were 500 μm in diameter, and the fluid properties were taken to be those of water and air. Droplets were allowed to enter the network from a circle centered in the network with equal diameter to the droplets themselves. (There was no attempt to mimic the dynamics or hydrostatics of the drop outside of the network.) Droplets entered the fiber at atmospheric pressure and spread in all directions (that is, laterally as well as into the fiber) as dictated by the dynamics of spontaneous imbibition.

Figure 11 contains images of the droplets after they had spread into the network. As in the previous figures, the shading corresponds to the fluid saturation averaged over the thin direction of the material. Figure 11a is the random, strongly wetting material. As one might expect, the drop spreads somewhat nonuniformly, although the favorable mobility ratio helps to damp this effect considerably. The presence of finite saturations away from the main droplet indicate that the model allowed for significant spreading through the wetting films; the reasonableness of this effect is addressed in the next section. Figure 11b is the same network, but with nearly neutral wettability. The rate of imbibition is much slower (see Figure 12), and there are no visual signs of transport through wetting films. While the shapes in Figures 11a and 11b are qualitatively similar, the specific differences are surprising, considering that the network structures are identical. The differences demonstrate the strong effect that wettability has on both rate and pattern of displacement. The pattern in Figure 11c is more uniform and circular, which is consistent with the more uniform fiber structure. The pattern in Figure 11d is elongated in the $\pm x$ directions, suggesting that spreading occurred preferentially along the directions of fiber orientation. It should be emphasized that the viscosity ratio for these displacements favors uniform front propagation, helping to negate effects of heterogeneity. Displacement processes consisting of liquid–liquid imbibition or the forced injection of air into water would exhibit much more dependence on structure. It should also be noted that, if the simulations were allowed to continue once the entire drop volume is imbibed, there would be continued spreading until an equilibrium configuration was achieved. This additional step in the modeling would require a simple change of boundary conditions once the entire droplet volume had imbibed into the network.

Transport in wetting films

The last topic to be addressed is the relative importance of transport in wetting films and the accuracy with which this can be predicted in network models. While the analysis of

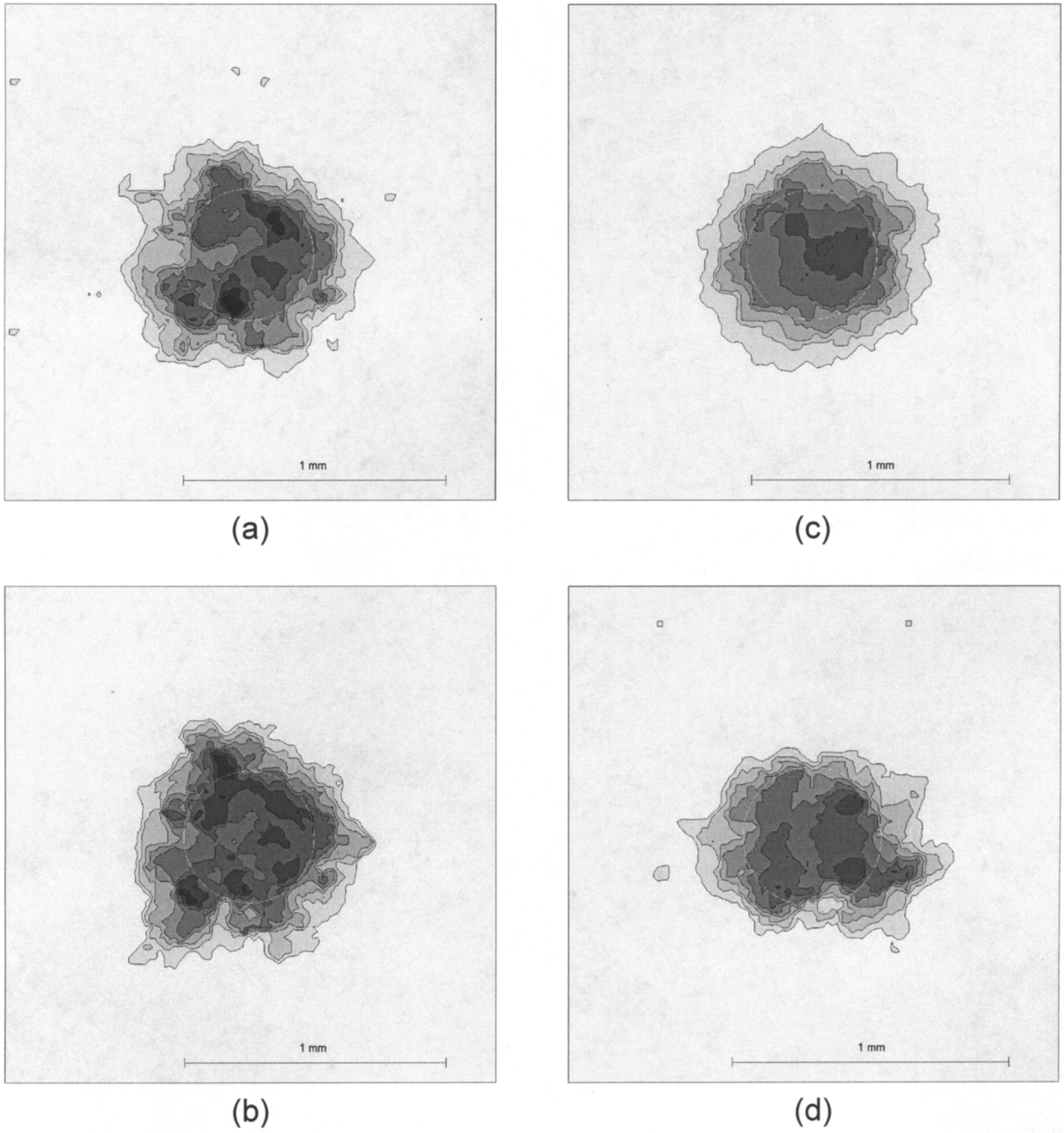

Figure 11. Images showing spontaneous imbibition of 0.5-mm-diameter water droplets into dry fibers having various structures and wettabilities.

Ransohoff and Radke (1988) is rigorous, it applies to simple geometries compared to most real porous materials. Furthermore, knowledge of the hydraulic conductivities within wetting films is only one factor in the problem. A second important consideration is how well connected the wetting-film network is. This second factor will ultimately dictate whether film transport can occur over multiple pore lengths.

In low-porosity consolidated rocks (especially with angular pore shapes), the formation of percolating networks of wetting films seems reasonable. In sphere packs, it is well known that pendular rings become isolated from one another at a finite wetting-phase saturation. One would suspect that the level of film interconnectivity within a fiber network is probably low, but dependent on porosity, pore structure, and of course saturation. Addressing these questions will require future experimental and numerical research. An important numerical issue is a sensitivity analysis of the model parameters that govern wetting-phase transport. The examples in this section provide a starting point for a more complete analysis of these numerical effects.

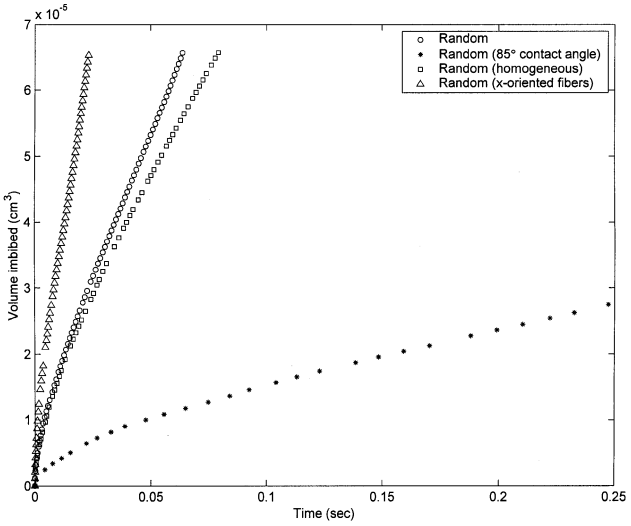

Figure 12. Imbibition rates for the four droplets shown in Figure 11.

We suspect that the current network model overpredicts the rate of fluid transport through wetting films because of the implicit assumption in the mathematics that the individual films are well connected. To help assess the sensitivity of macroscopic transport to the wetting-film hydraulic conductivity parameter in the model, simulations were performed comparing two sets of results: one set in which the hydraulic conductivities of wetting films were calculated as described previously, and one set in which these film conductivities were lowered by an arbitrary factor of 10. These comparisons were made for two displacement scenarios where wetting-film transport is important.

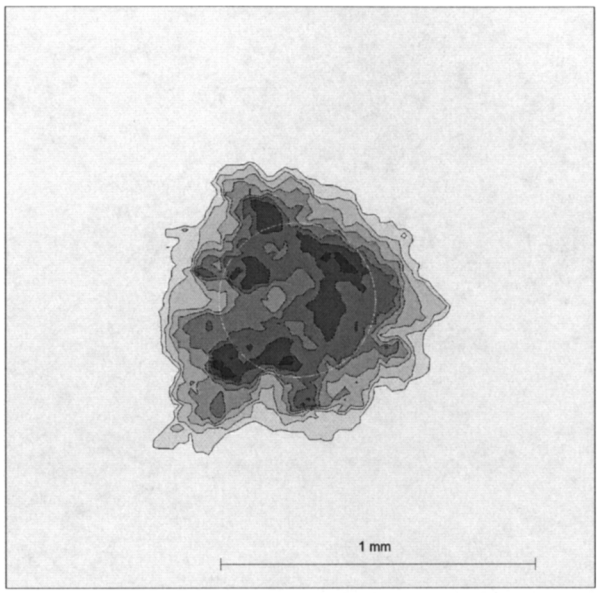

Figure 13. Drop pattern for the same conditions as shown in Figure 11a, but with a factor-of-10 lower wetting-film conductivity in the model.

The first displacement scenario is the drop-spreading process described in the previous section. In the random, water-wet fibrous material, water was observed to spread well past the bulk saturation front, which can be seen in Figure 11a. This simulation was repeated using the same porous material and wettability, but with film conductivities reduced by a factor of 10. Figure 13 contains the new image of the imbibed droplet, while Figure 14 is a plot of the imbibition rates for the two cases. Comparing the images (Figure 11a with Figure 13), the spreading pattern does have significant differences. Using the lower film conductivities, the saturation is more localized, which is not surprising. But, the pattern shape is much more similar to Figure 11b (the near-neutral-wettability case). This observation suggests that the conductivity of the films ahead of the front can have a significant effect on flow behind the front. Figure 14 indicates that, despite differences in fluid distribution in the fibrous material, only a slight difference in the overall imbibition rate occurred because of the change in film conductivity.

The second displacement scenario is a constant-flow-rate injection of air into a water-saturated fibrous material. Wetting-film transport is important in this process due to the slow drainage of wetting films once air has broken through to the outlet of the medium. In general, drainage processes can require hundreds of pore volumes to come to steady state, which is reached only when the pressure gradient in the wetting phase becomes zero (or it becomes disconnected). The simulations were performed on a small network of 250 pores because of the large computational requirements for the long-time drainage simulations. The rate of air injected was set equal to the approximate rate of spontaneous water imbibition into the same network, and two parameters were examined: the saturation and the inlet pressure, both vs. pore volumes injected. Figure 15 is a plot of the wetting-phase saturation. The tenfold difference in hydraulic conductivity caused about a 10% difference in the steady-state saturation that was achieved. (The simulations were extended to approxi-

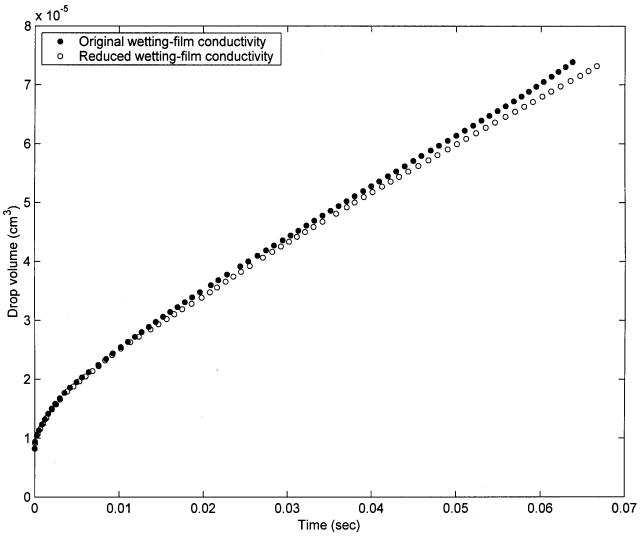

Figure 14. Net imbibition rates of 0.5-mm droplets: comparison of results for different wetting-film conductivities.

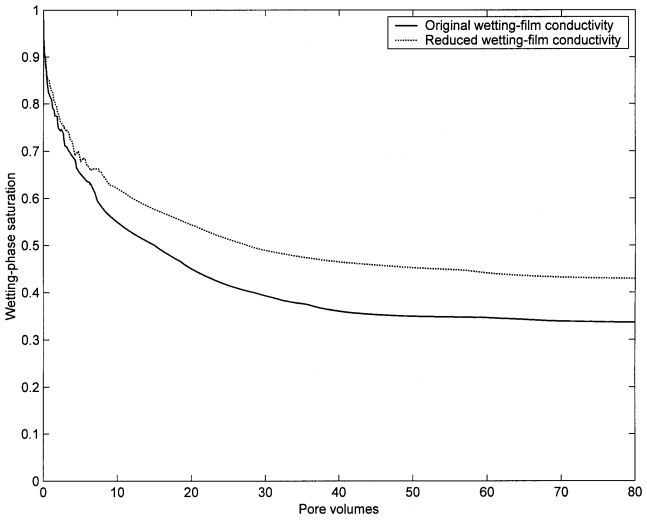

Figure 15. Long-time saturation profiles during displacement of water by air from a fibrous material.

mately 800 pore volumes, at which point the saturations had not changed significantly from the plateau values starting at 80 pore volumes.) Figure 16 is a plot of inlet nonwetting-phase pressure during displacement, normalized by the pressure drop for a single-phase flow of water at the same rate. It drops significantly during displacement because of the lower viscosity of air. The large fluctuations are caused by pressure increases (to gain access to small pore spaces), followed by pressure decreases during rapid interface advances and/or possible access to larger pores. Although some of the behavior can be attributed to the numerical algorithm, it is largely phenomenological in nature, albeit exaggerated by the relatively small-sized network. Comparing the two pressure profiles, the transients do not coincide exactly, but the average pressure behavior is essentially identical. That the 10% difference in saturation does not affect the nonwetting-phase conductivity suggests an important conclusion: the difference in wetting-phase saturation seen in Figure 15 can be attributed to swollen wetting films, not differences in the pore-scale invasion pattern.

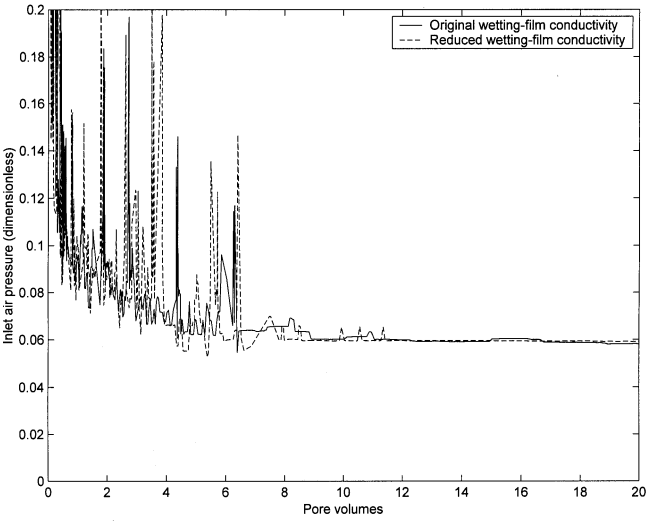

Figure 16. Inlet pressure during displacement of water by air from a fibrous material.

An observation common to both of these last examples is that the hydraulic conductivity of the wetting films affects details of the wetting-phase structure, but has a relatively small effect on bulk transport quantities such as pressure and rate. The wetting-phase structure is important for certain applications, and further research is certainly warranted to improve how film flow is quantified. However, encouragement can be taken from the fact that certain important transport parameters appear to be relatively insensitive to these microscopic details (such as rates and pressures in the cases presented).

Conclusions

Network modeling, which traditionally has been used for granular and consolidated media, has been adapted and tested for use with fibrous materials. Differences in the modeling approach reflect morphologic features that are found mainly in fibrous materials: orders-of-magnitude differences in solid-volume fraction, high-aspect-ratio particles, and anisotropy at the pore scale. Of particular significance are modifications to the network approach, which for the first time allow it to be used with very low solid-volume-fraction materials.

Prototype fibrous networks are based on random Voronoi diagrams. While they are not intended to mimic any one specific material, they provide a means to rapidly generate different fibrous structures, thereby allowing one to better understand the influence of morphologic features on fluid transport. Properties that can easily be controlled in the prototype networks are solid volume fraction, anisotropy, disorder, pore structure, and spatial correlation. Wettability (that is, contact angle) can be assigned independent of the network structure, either uniformly or at the pore scale.

Two fluid-flow algorithms are used with the current model. The first is quasi-static. The second is dynamic. The quasi-static algorithm is most useful for the rapid simulation of processes governed by interfacial forces. The dynamic algorithm is much more computationally intensive, but incorporates all relevant physics, and is therefore used for dynamic flow modeling in which viscous forces are significant. While the traditional engineering applications (for which network modeling has been used) are pressure-driven flows, capillary-driven imbibition is important in many applications where fibrous materials are involved. Hence, the model development and examples in this article focus largely on this mode of fluid transport.

The main advantage of quantitative network modeling is that it can be used in situations where the relevant continuum parameters for transport are not known. The inability to accurately predict continuum parameters is common (especially for multiphase flow), because of the complex interplay between viscous, gravity and pressure forces, and the strong influence of a medium's structure on the dynamics. The ex-

amples given in this article emphasize the predictive role of network modeling. Quantitative displacement behavior is predicted for a number of different cases, as a function of material structure, wettability, and fluid velocity.

The results in this article show that the network modeling approach is a powerful tool for fibrous materials, despite the significant morphologic differences between these and granular materials. Future research should focus on two important areas. The first is the generation of network structures that replicate real materials of interest. New techniques of this type will allow for better comparison with experimental results and foster further developments that are required to bring the modeling to a predictive level. The second topic is numerical upscaling techniques, which are needed to integrate pore-scale-modeling results with continuum models for transport.

Literature Cited

Bafna, S. S., and D. G. Baird, "An Impregnation Model for the Preparation of Thermoplastic Prepregs," *J. Compos. Mater.*, **26**, 683 (1992).

Bakke, S., and P. E. Oren, "3-D Pore-Scale Modelling of Sandstones and Flow Simulations in the Pore Networks," *SPE J.*, **2**, 136 (1997).

Blunt, M., and P. King, "Relative Permeabilities from Two- and Three-Dimensional Pore-Scale Network Modelling," *Transp. Porous Media*, **6**, 407 (1991).

Bryant, S. L., and M. Blunt, "Prediction of Relative Permeability in Simple Porous Media," *Phys. Rev. A*, **46**, 2004 (1992).

Bryant, S., A. Johnson, and R. Bonnecaze, "Influence of Wetting Phase Connectivity on Fluid-fluid Interfacial Area During Drainage of a Porous Medium," ACS Meeting, Washington, DC (2000).

Bryant, S. L., P. R. King, and D. W. Mellor, "Network Model Evaluation of Permeability and Spatial Correlation in a Real Random Sphere Packing," *Trans. in Porous Media*, **11**, 53 (1993a).

Bryant, S. L., D. W. Mellor, and C. A. Cade, "Physically Representative Network Models of Transport in Porous Media," *AIChE J.*, **39**, 387 (1993b).

Clague, D. S., and R. J. Phillips, "A Numerical Calculation of the Hydraulic Permeability of Three-Dimensional Disordered Fibrous Media," *Phys. Fluids*, **9**, 1562 (1997).

Coles, M. E., R. D. Hazlett, P. Spanne, W. E. Soll, E. L. Muegge, and K. W. Jones, "Pore Level Imaging of Fluid Transport Using Synchrotron X-Ray Microtomography," *J. Petrol. Sci. Eng.*, **19**, 55 (1998).

Dabros, T., "A Singularity Method for Calculating Hydrodynamic Forces and Particle Velocities in Low-Reynolds-Number Flows," *J. Fluid Mech.*, **156**, 1 (1985).

Dias, M. M., and A. C. Payatakes, "Network Models for Two-Phase Flow in Porous Media; Part 2. Motion of Oil Ganglia," *J. Fluid Mech.*, **164**, 337 (1986).

Dillard, L. A., and M. J. Blunt, "Development of a Pore Network Simulation Model to Study Nonaqueous Phase Liquid Dissolution," *Water Resour. Res.*, **36**, 439 (2000).

Drummond, J. E., and M. I. Tahir, "Laminar Viscous Flow Through Regular Arrays of Parallel Solid Cylinders," *Int. J. Multiphase Flow*, **10**, 515 (1984).

Dullien, F. A. L., *Porous Media, Fluid Transport and Pore Structure*, Academic Press, San Diego (1992).

Ethier, C. R., "Flow Through Mixed Fibrous Materials, *AIChE J.*, **37**, 1227 (1991).

Fatt, I., "The Network Model of Porous Media: I. Capillary Pressure Characteristics," *Pet. Trans. AIME*, **207**, 144 (1956).

Finney, J. L., "Random Packings and the Structure of Simple Liquids I. The Geometry of Random Close Packing," *Proc. Roy. Soc. London* **A. 319**, 479 (1970).

Fredd, C. N., and H. S. Fogler, "Influence of Transport and Reaction on Wormhole Formation in Porous Media," *AIChE J.*, **44**, 1933 (1998).

Ghassemzadeh, J., M. Hashemi, L. Sartor, and M. Sahimi, "Pore Network Simulation of Imbibition into Paper during Coating: 1. Model Development," *AIChE J.*, **47**, 519 (2001).

Goode, P. A., and T. S. Ramakrishnan, "Momentum Transfer Across Fluid-Fluid Interfaces in Porous Media: A Network Model," *AIChE J.*, **39**, 1124 (1993).

Gunstensen, A. K., and D. H. Rothman, "Lattice Boltzmann Studies of Immiscible Two-Phase Flow through Porous Media," *J. Geophys. Res.*, **98**, 6431 (1993).

Higdon, J. J. L., and G. D. Ford, "Permeability of Three-Dimensional Models of Fibrous Porous Media," *J. Fluid Mech.*, **308**, 341 (1996).

Hilpert, M., and C. T. Miller, "Pore-Morphology-Based Simulation of Drainage in Totally Wetting Porous Media," *Adv. Water Resour.*, **24**, 243 (2001).

Hoefner, M. L., and H. S. Fogler, "Pore Evolution and Channel Formation During Flow and Reaction in Porous Media," *AIChE J.*, **34**, 45 (1988).

Jackson, G. W., and D. F. James, "The Hydrodynamic Resistance of Hyaluronic Acid and its Contribution to Tissue Permeability," *Biorheology*, **19**, 317 (1982).

Jackson, G. W., and D. F. James, "The Permeability of Fibrous Porous Media," *Can. J. Chem. Eng.*, **64**, 364 (1986).

Jerauld, G. R., J. C. Hatfield, L. E. Scriven, and H. T. Davis, "Percolation and Conduction on Voronoi and Triangular Networks: A Case Study in Topological Disorder," *J. Phys. C. Solid State Phys.*, **17**, 1519 (1984).

Koch, D. L., and A. J. C. Ladd, "Moderate Reynolds Number Flows through Periodic and Random Arrays of Aligned Cylinders," *J. Fluid Mech.*, **349**, 31 (1997).

Koplik, J., "Creeping Flow in Two-Dimensional Networks," *J. Fluid Mech.*, **119**, 219 (1982).

Koplik, J., and T. J. Lasseter, "Two-Phase Flow in Random Network Models of Porous Media," *Soc. Pet. Eng. J.*, 89 (Feb., 1985).

Koplik, J., C. Lin, and M. Vermette, "Conductivity and Permeability from Microgeometry," *J. Appl. Phys.*, **56**, 3127 (1984).

Larson, R. E., and J. J. L. Higdon, "Microscopic Flow Near the Surface of Two-Dimensional Porous Media. Part 2. Transverse Flow," *J. Fluid Mech.*, **178**, 119 (1987).

Lenormand, R., E. Touboul, and C. Zarcone, "Numerical Models and Experiments on Immiscible Displacements in Porous Media," *J. Fluid Mech.*, **189**, 165 (1988).

Li, Y., and C.-W. Park, "A Predictive Model for the Removal of Colloidal Particles in Fibrous Filter Media," *Chem Eng. Sci.*, **54**, 633 (1999).

Liang, Z., M. A. Ioannidis, and I. Chatzis, "Permeability and Electrical Conductivity of Porous Media from 3D Stochastic Replicas of the Microstructure," *Chem. Eng. Sci.*, **55**, 5247 (2000).

Lindquist, W. B., S.-M. Lee, D. A. Coker, J. W. Jones, and P. Spanne, "Medial Axis Analysis of Void Structure in Three-Dimensional Tomographic Images of Porous Media," *J. Geophys. Res.*, **101**, 8297 (1996).

Liu, G., and K. E. Thompson, "A Domain Decomposition Method for Modeling Stokes Flow in Porous Materials," *Int. J. Numer. Meth. Fluids*, **38**, 1009 (2002).

Lowry, M. I., and C. T. Miller, "Pore-Scale Modeling of Nonwetting-Phase Residual in Porous Media," *Water Resour. Res.*, **31**, 455 (1995).

Martys, N. S., and H. Chen, "Simulation of Multicomponent Fluids in Complex Three-Dimensional Geometries by the Lattice Boltzmann Method," *Phys. Rev. E*, **53**, 743 (1996).

Mogensen, K., and E. Stenby, "A Dynamic Two-Phase Pore-Scale Model of Imbibition," *Transp. Porous Media*, **32**, 299 (1998).

Qi, D., "Microstructural Model for a Three-Dimensional Fiber Network," *TAPPI J.*, **80**, 283 (1997).

Qi, D., and T. Uesaka, "Numerical Experiments on Paper-Fluid Interaction—Permeabilitiy of a Three-Dimensional Anisotropic Fibre Network," *J. Mat. Sci.*, **34**, 4865 (1996).

Ransohoff, T. C., and C. J. Radke, "Laminar Flow of a Wetting Liquid Along the Corners of a Predominantly Gas-Occupied Noncircular Pore," *J. Colloid. Int. Sci.*, **121**, 392 (1988).

Sahimi, M., and T. T. Tsotsis, "Transient Diffusion and Conduction in Heterogeneous Media: Beyond the Classical Effective-Medium Approximation," *Ind. Eng. Chem. Res.*, **36**, 3043 (1997).

Sangani, A. S., and A. Acrivos, "Slow Flow Past Periodic Arrays of Cylinders with Applications to Heat Transfer," *Int. J. Multiphase Flow*, **8**, 193 (1982).
Sangani, A. S., and G. Mo, "Inclusion of Lubrication Forces in Dynamic Simulations," *Phys. Fluids*, **6**, 1653 (1994).
Sangani, A. S., and C. Yao, "Transport Processes in Random Arrays of Cylinders. II. Viscous Flow," *Phys. Fluids*, **31**, 2435 (1988).
Schweers, E., and F. Loffler, "Realistic Modelling of the Behaviour of Fibrous Filters through Consideration of Filter Structure," *Powder Technol.*, **80**, 191 (1994).
Shulmeister, V., M. W. D. Van der Burg, E. Van der Giessen, and R. Marissen, "Numerical Study of Large Deformations of Low-Density Elastomeric Open-Cell Foams," *Mech. Mat.*, **30**, 125 (1998).
Spanne, P., J. F. Thovert, C. J. Jacquin, W. B. Lindquist, K. W. Jones, and P. M Adler, "Synchrotron Computed Microtomography of Porous Media: Topology and Transports," *Phys. Rev. Lett.*, **73**, 2001 (1994).
Termonia, Y., "Permeability of Sheets of Nonwoven Fibrous Media," *Chem. Eng. Sci.*, **53**, 1203 (1998).
Thauvin, F., and K. K. Mohanty, "Network Modeling of Non-Darcy Flow Through Porous Media," *Transp. Porous Media*, **31**, 19 (1998).
Thompson, K. E., and H. S. Fogler, "Modeling Flow in Disordered Packed Beds from Pore-Scale Fluid Mechanics," *AIChE J.*, **43**, 1377 (1997).
Thompson, K. E., and H. S. Fogler, "A Pore-Scale Model for Fluid Injection and In-Situ Gelation in Porous Media," *Phys. Rev. E*, **57**, 5825 (1998).
Van Der Vorst, H. A., "BI-CGSTAB: A Fast and Smoothly Converging Variant of BI-CG for the Solution of Nonsymmetric Linear Systems," *SIAM J. Stat. Comput.*, **13**, 631 (1992).
Verberg, R., and A. J. C. Ladd, "Simulation of Low-Reynolds-Number Flow via a Time-Independent Lattice-Boltzmann Method," *Phys. Rev. E*, **60**, 3366 (1999).
Manuscript received May 1, 2001, and revision received Jan. 3, 2001.